University of Massachusetts Medical School

eScholarship@UMMS

Open Access Articles | Open Access Publications by UMMS Authors

2019-04-09

The ER-Localized Protein DFCP1 Modulates ER-Lipid Droplet Contact Formation

Dongfang Li
University of Chinese Academy of Sciences

Et al.

Let us know how access to this document benefits you.

Follow this and additional works at: https://escholarship.umassmed.edu/oapubs

 Part of the Amino Acids, Peptides, and Proteins Commons, Cell Biology Commons, Cells Commons, Developmental Biology Commons, Lipids Commons, and the Molecular Biology Commons

Repository Citation

Li D, Zhao YG, Li D, Zhao H, Huang J, Miao G, Feng D, Liu P, Li D, Zhang H. (2019). The ER-Localized Protein DFCP1 Modulates ER-Lipid Droplet Contact Formation. Open Access Articles. https://doi.org/10.1016/j.celrep.2019.03.025. Retrieved from https://escholarship.umassmed.edu/oapubs/3819

Creative Commons License

This work is licensed under a Creative Commons Attribution-Noncommercial-No Derivative Works 4.0 License.
This material is brought to you by eScholarship@UMMS. It has been accepted for inclusion in Open Access Articles by an authorized administrator of eScholarship@UMMS. For more information, please contact Lisa.Palmer@umassmed.edu.

Article

Cell Reports

The ER-Localized Protein DFCP1 Modulates ER-Lipid Droplet Contact Formation

Graphical Abstract

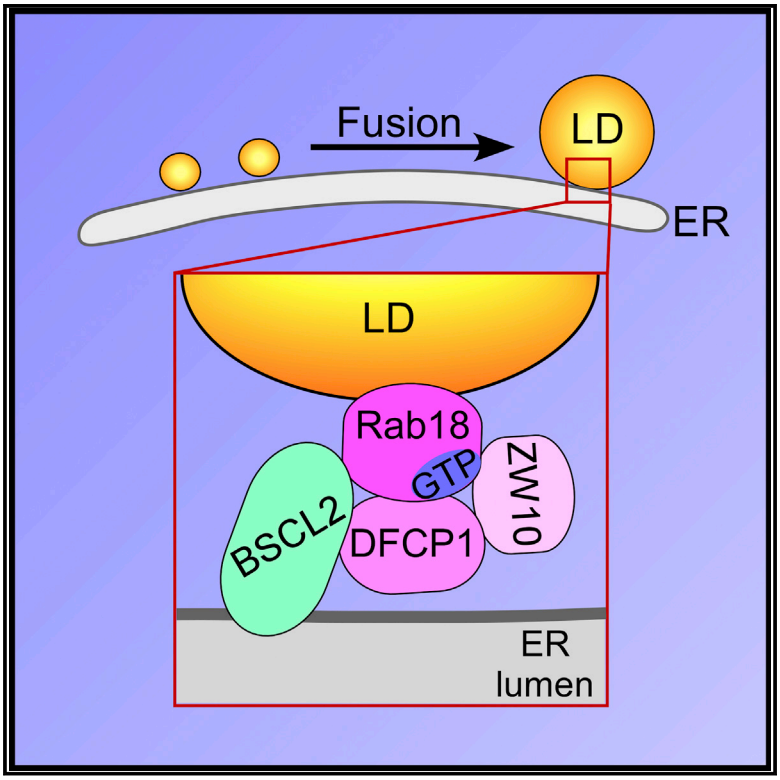

Highlights

- The ER protein DFCP1 redistributes from the ER to LDs upon induction of LD formation
- Fusion of DFCP1-labeled nascent structures contributes to initial LD growth
- BSCL2 regulates the dynamics and maturation of DFCP1-labeled structures
- DFCP1 interacts with the Rab18-ZW10 complex to mediate ER-LD contact formation

Authors

Dongfang Li, Yan G. Zhao, Di Li, ..., Pingsheng Liu, Dong Li, Hong Zhang

Correspondence

lidong@ibp.ac.cn (D.L.), hongzhang@ibp.ac.cn (H.Z.)

In Brief

Li et al. used super-resolution GI-SIM imaging to reveal that during LD biogenesis, the ER-localized protein DFCP1 redistributes to nascent LD structures, which further fuse to form expanding LDs. DFCP1 acts as a Rab18 effector for LD localization and interacts with the Rab18-ZW10 complex to mediate ER-LD contact formation.

Li et al., 2019, Cell Reports *27*, 343–358
April 9, 2019 © 2019 The Author(s).
https://doi.org/10.1016/j.celrep.2019.03.025

CellPress

Cell Reports
Article

OPEN ACCESS
CellPress

The ER-Localized Protein DFCP1 Modulates ER-Lipid Droplet Contact Formation

Dongfang Li,[1,2,5] Yan G. Zhao,[3,5] Di Li,[1] Hongyu Zhao,[1] Jie Huang,[1] Guangyan Miao,[1] Du Feng,[4] Pingsheng Liu,[1] Dong Li,[1,2,*] and Hong Zhang[1,2,6,*]

[1]National Laboratory of Biomacromolecules, CAS Center for Excellence in Biomacromolecules, Institute of Biophysics, Chinese Academy of Sciences, Beijing 100101, China
[2]College of Life Sciences, University of Chinese Academy of Sciences, Beijing 100049, China
[3]Department of Molecular, Cell and Cancer Biology, University of Massachusetts Medical School, Worcester, MA 01605, USA
[4]School of Basic Medical Sciences, Guangzhou Medical University, Guangzhou 511436, China
[5]These authors contributed equally
[6]Lead Contact
*Correspondence: lidong@ibp.ac.cn (D.L.), hongzhang@ibp.ac.cn (H.Z.)
https://doi.org/10.1016/j.celrep.2019.03.025

SUMMARY

Very little is known about the spatiotemporal generation of lipid droplets (LDs) from the endoplasmic reticulum (ER) and the factors that mediate ER-LD contacts for LD growth. Using super-resolution grazing incidence structured illumination microscopy (GI-SIM) live-cell imaging, we reveal that upon LD induction, the ER-localized protein DFCP1 redistributes to nascent puncta on the ER, whose formation depends on triglyceride synthesis. These structures move along the ER and fuse to form expanding LDs. Fusion and expansion of DFCP1-labeled nascent structures is controlled by BSCL2. *BSCL2* depletion causes accumulation of nascent DFCP1 structures. DFCP1 overexpression increases LD size and enhances ER-LD contacts, while *DFCP1* knockdown has the opposite effect. DFCP1 acts as a Rab18 effector for LD localization and interacts with the Rab18-ZW10 complex to mediate ER-LD contact formation. Our study reveals that fusion of DFCP1-labeled nascent structures contributes to initial LD growth and that the DFCP1-Rab18 complex is involved in tethering the ER-LD contact for LD expansion.

INTRODUCTION

The lipid droplet (LD) consists of neutral lipids (e.g., triglycerides and sterol esters) that are enwrapped by a phospholipid monolayer (Yang et al., 2012; Joshi et al., 2017; Walther et al., 2017). The LD surface is decorated with proteins that regulate lipid storage, metabolism, and movement of droplets (Kory et al., 2016). LDs originate from the endoplasmic reticulum (ER), and their formation involves discrete steps (Kassan et al., 2013; Wang et al., 2016). Neutral lipids synthesized in the ER bilayer membrane accumulate to form lens-like structures (Choudhary et al., 2015; Walther et al., 2017; Qi et al., 2017). The growing droplet progressively distends the ER membrane and eventually buds off into the cytoplasm to form a nascent LD (Choudhary et al., 2015; Walther et al., 2017; Qi et al., 2017). The egress of neutral lipids from the bilayer membrane and LD budding is specified by the ER phospholipid composition and surface tension (Ben M'barek et al., 2017; Choudhary et al., 2018). The ER transmembrane protein FIT2 (fat-storage-inducing transmembrane) facilitates the emergence of LDs from the ER, probably by regulating diacylglycerol (DAG) levels at the sites of LD biogenesis (Choudhary et al., 2015). Very little is known about the dynamics of the initial stage of LD formation. For example, whether a nascent LD is generated from individual neutral lipid-containing LD precursors or involves fusion of LD precursors remains unknown.

Nascent LDs, which may be connected to the ER or separated completely from it, reengage with the ER for expansion. LDs form contacts with the ER, in which two membranes are closely apposed (typically within 30 nm) and/or are physically connected with the ER by narrow membrane stalks. At the contact sites and membrane extensions, neutral lipids synthesized in the ER are transported to LDs for growth (Walther et al., 2017; Joshi et al., 2017). ER-resident biosynthetic enzymes for neutral lipids, such as GPAT4 and DGAT2, also transfer from the ER to the LD surface via membrane connections for local lipid synthesis (Wilfling et al., 2013). Lipolysis of LDs also induces ER-LD contacts for back transport of phospholipids and droplet proteins to the ER (Kory et al., 2016). LD growth can also result from fusion of LDs, which rarely occurs under normal conditions. Fusion of LDs is facilitated by phosphatidylcholine (PC) deficiency, phosphatidic acid (PA) accumulation, or expression of the LD-localized protein Fsp27 (Fei et al., 2011; Krahmer et al., 2011; Gong et al., 2011).

Membrane contact sites (MCSs) are established by protein-protein and/or protein-phosphoinositide interactions between the two opposing membranes (Phillips and Voeltz, 2016). Several factors have been identified that are involved in the formation and/or maintenance of ER-LD contact. The lipid synthesis enzymes FATP1 (acetyl coenzyme A [acyl-CoA] synthetase) and DGAT2 (diacylglycerol acyltransferase), which are located on the ER and the LD, respectively, have been shown to form a complex to tether the ER to LDs, thus coupling the synthesis and deposition of triglycerides (TGs) into LDs (Xu et al., 2012). The GTP-bound form of Rab18 interacts with the NRZ tethering

This is an open access article under the CC BY-NC-ND license (http://creativecommons.org/licenses/by-nc-nd/4.0/).

factors (NAG-RINT1-ZW10) and their associated ER-localized SNAREs (Use1, Syntaxin18, and BNIP1) to promote the formation of ER-LD contacts for LD growth in preadipocytes (Xu et al., 2018). The formation of membrane bridges between LDs and the ER is promoted by the Arf1-coatomer protein (COP) I machinery, which removes phospholipids from the LD surface and in turn increases LD surface tension (Thiam et al., 2013; Wilfling et al., 2014). The stability of ER-LD contact is modulated by the ER-localized transmembrane protein EPG-3 (also known as VMP1), which activates the calcium transporter SERCA (Zhao et al., 2017). The ER-resident transmembrane protein BSCL2, encoded by human Berardinelli-Seip congenital lipodystrophy 2, forms discrete foci at ER-LD contacts and controls the growth of nascent LDs to large mature LDs (Wang et al., 2016; Salo et al., 2016). *BSCL2* depletion causes accumulation of a large number of nascent LDs (not labeled by lipid dyes), clusters of small LDs, and a few supersized LDs (Wang et al., 2016; Salo et al., 2016). The supersized LDs result from aberrant targeting of lipid synthesis enzymes and/or LD coalescence due to changes in phospholipid composition (Wang et al., 2016; Salo et al., 2016; Wolinski et al., 2015). In *BSCL2*-depleted cells, ER-LD contacts are heterogeneous and morphologically irregular (Salo et al., 2016). How BSCL2 participates in the formation, function, and/or stabilization of ER-LD contacts remains largely unknown.

The ER also plays a pivotal role in the formation of the double-membrane autophagosome in higher eukaryotes (Zhao and Zhang, 2018). Upon autophagy induction, the Atg14L-Vps34 phosphatidylinositol 3-phosphate (PI(3)P) kinase complex is targeted to the ER to synthesize PI(3)P (Itakura and Mizushima, 2010). The PI(3)P-enriched ER subdomains, known as omegasomes, act as platforms for autophagosome formation (Axe et al., 2008). The omegasome extensively contacts and also forms membrane extensions with the isolation membrane (IM; autophagosomal precursor) during its expansion into an autophagosome (Zhao and Zhang, 2018). The FYVE-domain-containing ER-localized protein DFCP1 (also known as ZFYVE1) migrates to omegasomes upon autophagy induction, a process that depends on both the ER localization domain and the PI(3)P-binding FYVE domain (Axe et al., 2008). DFCP1 does not move to IMs, and it migrates back to the ER when the IM closes into the autophagosome (Axe et al., 2008). Although DFCP1 labels omegasomes, its knockdown (KD) causes no evident autophagy defects (Axe et al., 2008). DFCP1 is also identified as a component of the LD proteome (Bersuker et al., 2018), but its function in LD metabolism remains unknown.

Using a newly developed super-resolution live-cell imaging technique, we demonstrated that upon LD induction, DFCP1 forms small puncta on the ER in a manner that depends on TG synthesis. These DFCP1-labeled nascent structures move along the ER and fuse to form an expanding LD, which further grows into a large LD. BSCL2 is required for fusion and growth of DFCP1-labeled nascent structures. *DFCP1* KD reduces, while DFCP1 overexpression enhances, ER-LD contacts. DFCP1 acts as a Rab18 effector and interacts with the Rab18-ZW10 complex to mediate ER-LD contact. Our study reveals that initial LD growth involves fusion of nascent DFCP1-labeled structures, and LD expansion is modulated by the DFCP1-mediated ER-LD contact.

RESULTS

DFCP1 Relocates from the ER to LDs upon LD Induction

Under normal conditions, GFP-DFCP1 colocalized with the ER markers RFP-Sec61β and DsRed-KDEL (Figures 1A and S1A) (Axe et al., 2008). After 6-h oleic acid (OA) treatment, DFCP1 tightly enclosed LDs stained by LipidTOX, and the fluorescence intensity of GFP-DFCP1 on the ER was concomitantly decreased in COS7 and HeLa cells (Figures 1B, S1B, and S1C). GFP-DFCP1 fluorescence was enriched at LD-LD contact sites compared to other regions of LDs (Figures 1B and S1B–S1E). DFCP1-RFP also colocalized with the LD markers ACSL3 and GPAT4 after 6-h OA treatment (Figures 1C and S1F). Biochemical fractionation assays revealed that endogenous DFCP1 protein was present in purified LDs (Figure S1G). Levels of DFCP1 mRNA and proteins did not change after OA treatment (Figures S1H and S1I). We reconstructed the LD surface in three dimensions (3D) from deconvoluted structured illumination microscopy (SIM) images of LDs labeled by DFCP1 and found that DFCP1 was on the LD surface and tightly enwrapped the lipids (Figure 1D; Video S1).

The localization of DFCP1 was further determined by immunoelectron microscopy (EM) analysis. Gold particles recognizing GFP-DFCP1 specifically localized on the phospholipid monolayer surrounding LDs but were barely detected on the ER membrane (Figure 1E). More gold particles accumulated at LD-LD contact sites (Figure 1F). We also visualized the localization of DFCP1 using the chimeric APEX2-DFCP1 protein. APEX2 is an engineered peroxidase that catalyzes the formation of a highly electron-dense substance in the presence of diaminobenzidine (DAB) and OsO_4, thus facilitating the EM analysis of protein localization (Lam et al., 2015). Dark APEX2-DFCP1 signals were detected at the surface of LDs and the signal was stronger at LD-LD contact sites (Figures S1J and S1K). Taken together, these results show that DFCP1 redistributes from the ER to LDs after OA treatment.

We performed fluorescence recovery after photobleaching (FRAP) assays to examine the mobility of DFCP1 on LDs. After 6-h OA treatment, the GFP-DFCP1 fluorescence signal was bleached on a portion of the LD. We found that the GFP signal recovered within 2 s (Figures 1G and 1H). Recovery of the DFCP1 signal was also observed after bleaching of an entire LD (either a single LD or an LD within a cluster; Figures 1G and 1H). Thus, DFCP1 on the LD is mobile and exchanges with the ER and/or cytosol pool of DFCP1.

LD Localization of DFCP1 Depends on the ER Targeting Domain and the FYVE Domain

DFCP1 contains an ER targeting domain and also a phosphoinositide-binding FYVE domain (Figure S2A). We treated the membrane fraction of cellular extracts with high pH (pH 11.5) or high-salt (0.5 M NaCl) buffers and found that endogenous DFCP1 was present in the supernatant but absent in the pellet (membrane fraction), suggesting that DFCP1 is not an integral transmembrane ER protein (Figure S2B). The mutation GFP-DFCP1(W543A), which disrupts the ER localization of DFCP1 (Axe et al., 2008), prevented DFCP1 from anchoring onto LDs (Figure 1I). ER(DFCP1)-GFP, containing only the ER targeting

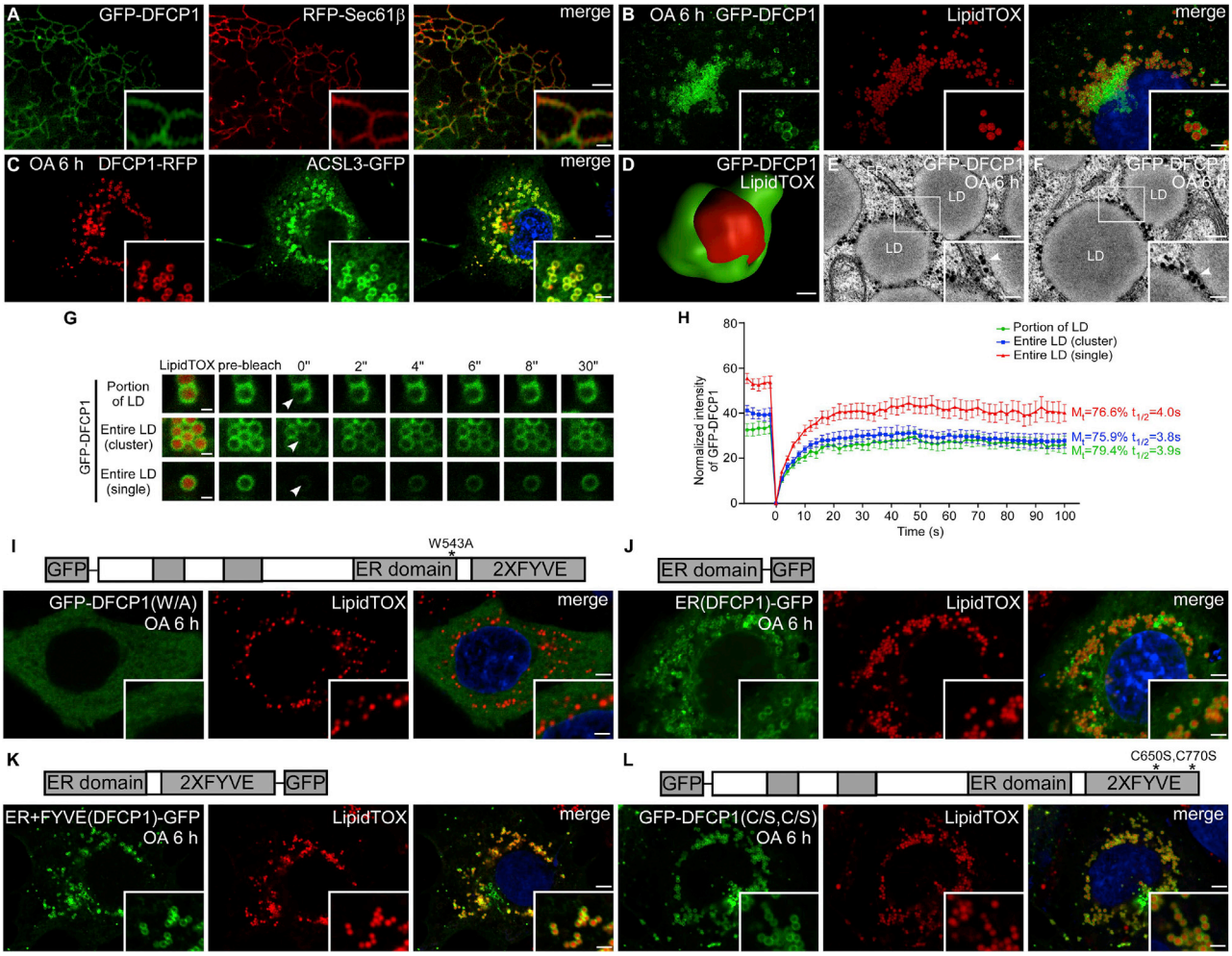

Figure 1. The ER-Localized Protein DFCP1 Moves to LDs upon LD Induction in a Manner Dependent on Its ER-Targeting Domain and FYVE Domain

(A) GI-SIM images reveal that under normal conditions, GFP-DFCP1 colocalizes with the ER marker RFP-Sec61β. Scale bar, 2 μm (insert, 400 nm). The experiments were performed in COS7 cells unless otherwise stated.

(B) SIM analysis shows that GFP-DFCP1 encloses LipidTOX-stained LDs. The fluorescence intensity is stronger at LD-LD contact sites.

(C) DFCP1-RFP colocalizes with ACSL3-GFP on LDs after 6-h OA treatment.

(B and C) Scale bars, 5 μm (inserts, 2 μm).

(D) 3D-SIM image shows that DFCP1 tightly enwraps an LD. Weak GFP-DFCP1 signals on LDs failed to be reconstituted in 3D-SIM images. Scale bar, 200 nm.

(E and F) Immuno-EM analysis reveals that after 6-h OA treatment, gold particles (white arrowheads), indicating GFP-DFCP1, localize on the LD surface (E) and are enriched at the contact sites (F). Scale bars, 200 nm (inserts, 100 nm).

(G) After 6-h OA treatment in HeLa cells, the fluorescence signal of GFP-DFCP1 recovered after photobleaching. Arrowheads indicate the site where the GFP signal was photobleached. Scale bars, 1 μm.

(H) The graph shows the time-dependent recovery of GFP-DFCP1 fluorescence on LDs after photobleaching in HeLa cells treated with OA for 6 h (n = 6 LDs for each independent experiment). M_f indicates the proportion of bleached protein that is replaced by unbleached protein during the recovery monitoring period; $t_{1/2}$ is the half-time of recovery, i.e., the time that the fluorescence reaches half of its maximal recovery intensity. Mean ± SEM is shown.

(I) GFP-DFCP1(W543A) fails to anchor on LDs.

(J) The ER targeting domain of DFCP1 (aa 416–543) labels LDs.

(K) The signal from ER+FYVE(DFCP1)-GFP on LDs is as strong as full-length DFCP1.

(L) GFP-DFCP1(C650S and C770S) encloses LDs.

In (I)–(L), schematic structures of the mutant DFCP1 proteins are shown on top. The mutation site in (I and L) is indicated by an asterisk (*). Scale bars, 5 μm (inserts, 2 μm) (I–L).

See also Figures S1 and S2.

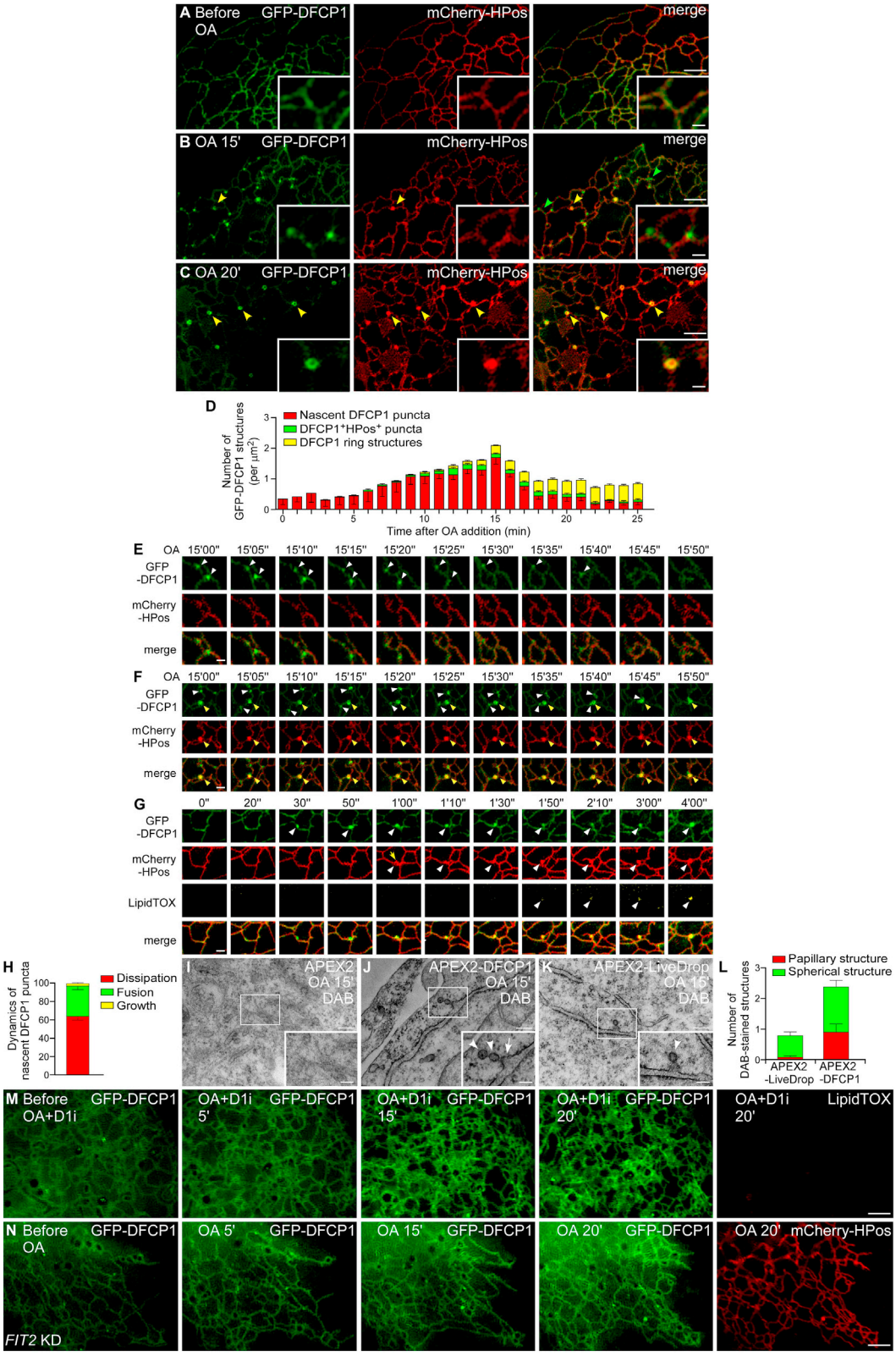

(legend on next page)

domain of DFCP1, labeled LDs after OA treatment, but the fluorescence signal on the LD was weaker than that of DFCP1 (Figure 1J). Chimeric proteins containing the ER-targeting domain of DFCP1 and the FYVE domain derived from DFCP1 or FENS, ER+FYVE(DFCP1) and ER(DFCP1)+FYVE(FENS), exhibited a strong GFP signal on the LD, like full-length DFCP1 (Figures 1K and S2C). Compared to DFCP1 and ER+FYVE(DFCP1), the half-time for recovery of the ER(DFCP1)-GFP fluorescence signal after photobleaching on LDs and the ER was shorter (Figures S2D–S2G). Thus, the FYVE domain contributes to the retention of DFCP1 on LDs.

Upon autophagy induction, DFCP1 moves to omegasomes in a manner that depends on the binding of PI(3)P to the FYVE domain and is abolished by wortmannin treatment (Axe et al., 2008). After OA treatment for 6 h, DFCP1 still colocalized with LC3 puncta upon starvation (Figure S2H). The LD localization of DFCP1, however, persisted after wortmannin treatment (Figure S2I). Mutations in the FYVE domain residues that are critical for PI(3)P binding, C650S and C770S (Axe et al., 2008), did not prevent DFCP1 from localizing to LDs (Figure 1L). Thus, PI(3)P is not required for the redistribution of DFCP1 from the ER to LDs. FYVE(FENS)-TM(CytoB5)-GFP, in which the bilayer-spanning ER domain from CytoB5 is linked to the FYVE domain of FENS, labels the omegasome (Axe et al., 2008). However, it failed to be recruited to LDs (Figure S2J). These results indicate that the ER-targeting domain and FYVE domain mediate the LD localization of DFCP1.

DFCP1 Labels Nascent LD Structures on the ER that Move and Fuse to Form an Expanding LD at the Early Stages of LD Biogenesis

We used grazing incidence structured illumination microscopy (GI-SIM) to examine the spatiotemporal recruitment of GFP-DFCP1 to LDs upon OA treatment. Compared to spinning-disk confocal microscopy or commercial SIM systems, GI-SIM provides a higher spatiotemporal resolution of 95 nm and 40 frames per second. Moreover, its axial illumination depth reaches ~1 μm, enabling us to examine the dynamics of subcellular organelles (Nixon-Abell et al., 2016). Formation of LDs at different stages can be monitored by different assays. LipidTOX stains LDs with a moderate amount of neutral lipid accumulation. HPos (containing the ER-anchoring hydrophobic domain of ALDI and the LD-targeting motif of caveolin-1) translocates from the ER to LDs before lipid accumulation can be stained by neutral lipid dyes (e.g., LipidTOX and BODIPY) (Kassan et al., 2013) and thus serves as a marker to detect the early stages of LD formation.

Time-lapse analysis using GI-SIM was performed to examine the temporal relationship of GFP-DFCP1 with mCherry-HPos. Before OA addition, GFP-DFCP1 colocalized with the ER marker RFP-Sec61β or mCherry-HPos on the ER (Figures 1A and 2A). After OA treatment for ~5 min, GFP-DFCP1 started to form a few new puncta, which were negative for mCherry-HPos, on the ER (Figure S3A). The number of DFCP1 puncta continued to increase up until 15 min (Figures 2B and 2D). A fraction of DFCP1 puncta became positive for mCherry-HPos (Figures 2B and 2D). After OA treatment for 20 min, only a few small DFCP1 puncta were present, but the GFP-DFCP1$^+$ mCherry-HPos$^+$ puncta gradually enlarged and became ring-like structures that continued to grow (Figures 2C, 2D, S3B, and S3C). During LD formation, the GFP-DFCP1 signal intensity on the LD increased (Figure S3D).

We further analyzed the dynamics of DFCP1 puncta. 64.1% of DFCP1 puncta dissipated into the ER (Figures 2E and 2H; Video S2), indicating that punctum formation is reversible. 33.1% of the DFCP1 puncta rapidly moved along the ER and fused with each

Figure 2. Dynamics of DFCP1-Labeled LD Structures during the Early Stages of LD Biogenesis

(A) GI-SIM images show that before OA treatment, GFP-DFCP1 colocalizes with mCherry-HPos on the ER.

(B) After 15-min OA treatment, GFP-DFCP1 colocalizes with mCherry-HPos on the ER. Some GFP-DFCP1 puncta colocalizes with mCherry-HPos (yellow arrowheads in all three panels indicate the same punctum) at three-way junction sites of the ER.

(C) After OA treatment for 20 min, almost all GFP-DFCP1 puncta colocalize with mCherry-HPos (yellow arrowheads).

(A–C) Scale bars, 2 μm (inserts, 400 nm).

(D) Quantification of the number of different types of GFP-DFCP1 structures at different time points after OA treatment. n = 13 areas of 10 μm^2 from 5 cells were examined for each time point. Data are shown as mean ± SEM.

(E) GI-SIM images at a series of time-points after OA addition show that DFCP1$^+$HPos$^-$ puncta (arrowheads in the top panel) decrease in intensity and gradually disappear into the ER. Scale bar, 400 nm.

(F) GI-SIM images at a series of time points after the addition of OA show that DFCP1$^+$HPos$^-$ puncta (white arrowheads in the top panel) move alone the ER and fuse with a nearby DFCP1$^+$HPos$^+$ punctum (yellow arrowhead) at the ER three-way junction site. Scale bar, 800 nm.

(G) The sequential order of punctum labeling by GFP-DFCP1, mCherry-HPos, and LipidTOX. 0′′ refers to the time point for analysis, not the onset of OA treatment. 63.3% of GFP-DFCP1$^+$ mCherry-HPos$^+$ puncta are localized at ER three-way junction (yellow arrow) (n = 79 puncta in 4 cells). Arrowheads indicate the emergence of each marker at the same punctum on the ER. Scale bar, 800 nm.

(H) Dynamics of nascent DFCP1 puncta during early stage of LD biogenesis (n = 8 areas of 10 μm^2 from 4 cells were examined within 25-min OA treatment). Data are shown as mean ± SEM.

(I–K) EM images of cells expressing APEX2 (I), APEX2-DFCP1 (J), and APEX2-LiveDrop (K). DAB does not stain the ER membrane in APEX2-expressing control cells (I). The DAB-stained papillary structure on the ER is indicated by arrow. Arrowheads indicate spherical structures adjacent to the ER. Scale bars, 200 nm (inserts, 100 nm).

(L) The number of DAB-stained structures in cells expressing APEX2-LiveDrop and APEX2-DFCP1 (n = 14 and 17 areas of 2 μm^2 from EM images, respectively, were examined after OA treatment for 15 min). Data are shown as mean ± SEM.

(M) Treatment with the DGAT1 inhibitor D1i suppresses the formation of nascent DFCP1 puncta after OA treatment.

(N) The number of nascent DFCP1 puncta decreases in *FIT2* KD cells after OA treatment.

(M and N) Scale bars, 2 μm.

See also Figure S3.

other and/or a DFCP1 punctum that was already positive for mCherry-HPos or LipidTOX, resulting in growth of the puncta (Figures 2F, 2H, and S3E; Video S2). 63.3% of GFP-DFCP1$^+$ mCherry-HPos$^+$ puncta were formed at three-way junctions of ER tubules (Figure 2G). Some DFCP1 puncta also detached from, and then migrated back to, the ER (Figure S3F). 2.8% of DFCP1 puncta grew into LDs that were stained by LipidTOX (Figure 2H). We also determined the dynamics of GFP-DFCP1, mCherry-HPos, and LipidTOX upon OA treatment. After OA treatment, GFP-DFCP1 puncta first emerged on the ER and then became mCherry-HPos positive. The puncta were then gradually stained by LipidTOX (Figure 2G). The DFCP1 puncta negative for LipidTOX staining are named hereafter as nascent DFCP1 puncta.

The resolution of GI-SIM could not differentiate between structures on the ER or adjacent (<100 nm) to the ER. We performed EM analysis to further characterize DFCP1 structures at early stages of LD biogenesis. After OA treatment for 15 min, in APEX2-DFCP1-expressing cells, DAB stained small papillary structures on the ER and also spherical structures (<100 nm) adjacent to the ER (Figures 2I, 2J, and 2L). Formation of puncta positive for LiveDrop, a widely used nascent LD marker (Wang et al., 2016), occurred later than DFCP1 (Figure S3G). APEX2-LiveDrop labeled spherical structures (<100 nm) close to the ER but only a few papillary structures (Figures 2K and 2L).

To further determine whether DFCP1 puncta represent early LD structures, we treated cells with the TG synthesis inhibitor D1i, which inhibits DGAT1 activity. We found that formation of nascent DFCP1 puncta was almost abolished (Figure 2M). FIT2 regulates emergence of LDs from the ER. *FIT2* KD causes a dramatic reduction in the number and size of LDs (Choudhary et al., 2015). Knocking down *FIT2* dramatically reduced the formation of nascent DFCP1 puncta (Figures 2N and S3H), suggesting that DFCP1-labeled structures are LD precursors. Taken together, these results indicate that DFCP1 is an earlier LD marker than mCherry-HPos and labels nascent LD structures, which fuse to form expanding LDs.

BSCL2 Controls Dissipation and Fusion of DFCP1-Labeled Nascent LDs

BSCL2 acts at the ER-LD contact site to regulate LD biogenesis (Wang et al., 2016; Salo et al., 2016). After 6-h OA treatment, BSCL2-GFP or endogenous BSCL2 formed distinct puncta that associate with LDs in control cells (Wang et al., 2016; Salo et al., 2016) (Figures S4A and S4C). In cells expressing mCherry-DFCP1, BSCL2-GFP, or endogenous BSCL2 closely encircled DFCP1-labeled LDs (Figures S4B and S4D). We knocked down *BSCL2* by RNAi in COS7 and HeLa cells to examine whether BSCL2 regulates the dynamics of DFCP1 puncta during LD formation (Figures S4E–S4G). After 6-h OA treatment, the number of GFP-DFCP1 puncta was much greater, while the localization of DFCP1 on LipidTOX-stained LDs was weaker, in *BSCL2* KD cells than in negative control (NC) cells (Figures 3A, 3B, S4H, and S4I). *BSCL2* depletion also suppressed the LD localization of ER(DFCP1)-GFP (Figures S4J and S4K). These results indicate that BSCL2 regulates DFCP1 targeting to mature LDs.

We next performed time-lapse analysis using GI-SIM to determine the spatiotemporal formation of DFCP1 puncta in *BSCL2* KD cells. Before addition of OA, ER localization of DFCP1 was weaker in *BSCL2* KD cells than in NC cells (Figures 3C and S4L), suggesting that BSCL2 regulates the ER association of DFCP1. After OA treatment, nascent DFCP1 puncta emerged from the ER in *BSCL2* KD cells (Figures 3D–3F and 3H). In control cells, GFP-DFCP1$^+$mCherry-HPos$^-$ puncta matured into GFP-DFCP1$^+$mCherry-HPos$^+$ puncta and then grew into ring structures (Figures 2G and S3C), while in *BSCL2* KD cells, fewer GFP-DFCP1$^+$mCherry-HPos$^+$ puncta grew into ring structures (Figures 3D–3F and 3H). GFP-DFCP1$^+$mCherry-HPos$^-$ puncta were able to move to the ER three-way junctions in *BSCL2* KD cells and become GFP-DFCP1$^+$mCherry-HPos$^+$ puncta (Figure 3G; Video S3). However, they were not stably anchored at the three-way junction. The GFP-DFCP1$^+$mCherry-HPos$^-$ puncta migrated away (Figure 3G; Video S3). In *BSCL2* KD cells, GFP-DFCP1$^+$mCherry-HPos$^+$ puncta sometimes formed clusters at the ER three-way junction, but the clusters were irregularly shaped and failed to grow in size (Figure S4M; Video S3). The dissipation of GFP-DFCP1$^+$mCherry-HPos$^-$ puncta into the ER was also inhibited in *BSCL2* KD cells (Figure 3I; Video S3). Therefore, a large number of nascent GFP-DFCP1 puncta persisted even after 20-min OA treatment in *BSCL2* KD cells (Figures 3F and 3H). *BSCL2* KD cells also contained a few GFP-DFCP1$^+$mCherry-HPos$^+$ ring structures, with which nascent DFCP1 puncta could fuse (Figure S4N). The growth of these LD structures was faster than in control cells (Figure S4O). However, the increase in DFCP1 fluorescence intensity on LDs was less in *BSCL2* KD cells (Figures S4O and S4P). Depletion of *BSCL2* resulted in accumulation of nascent LDs, which were not stained by LipidTOX (Wang et al., 2016). *BSCL2* KD cells contain both small and supersized LipidTOX-positive LDs (Wang et al., 2016; Salo et al., 2016) (Figures S4Q and S4R). EM analysis showed that APEX2-DFCP1 strongly labeled nascent LDs (<100 nm), but not small and supersized LDs (~300 nm and ~1 μm, respectively) in *BSCL2* KD cells (Figure 3J). Therefore, BSCL2 is required for the maturation of DFCP1-labeled nascent LDs into LipidTOX-positive mature LDs.

DFCP1 Regulates the Size of LDs

We next investigated the role of DFCP1 in LD biogenesis. *DFCP1* was knocked down by small interfering RNA (siRNA) in COS7 and HeLa cells (Figures S5A and S5B). After 6-h OA treatment, the average size of LDs was 0.78 μm in control COS7 cells and 1.45 μm in control HeLa cells, which was reduced to 0.65 μm and 1.18 μm in *DFCP1* KD cells, respectively (Figures 4A–4C and S5C–S5E). The number of LDs increased in *DFCP1* KD cells (Figures 4D and S5F). Compared to control mouse embryonic fibroblasts (MEFs), LDs were also smaller and more abundant in *DFCP1* KO MEFs (Figures S5A and S5G–S5J). In contrast to *DFCP1* KD, overexpression of GFP-DFCP1 increased the size of LDs (Figures 4E–4G). LDs also formed clusters in DFCP1-overexpressing cells (Figure 4F). Overexpression of ER(DFCP1) and ER+FYVE(DFCP1) also increased LD size (Figures 4G, S5K, and S5L). These results indicate that DFCP1 regulates the size and distribution of LDs.

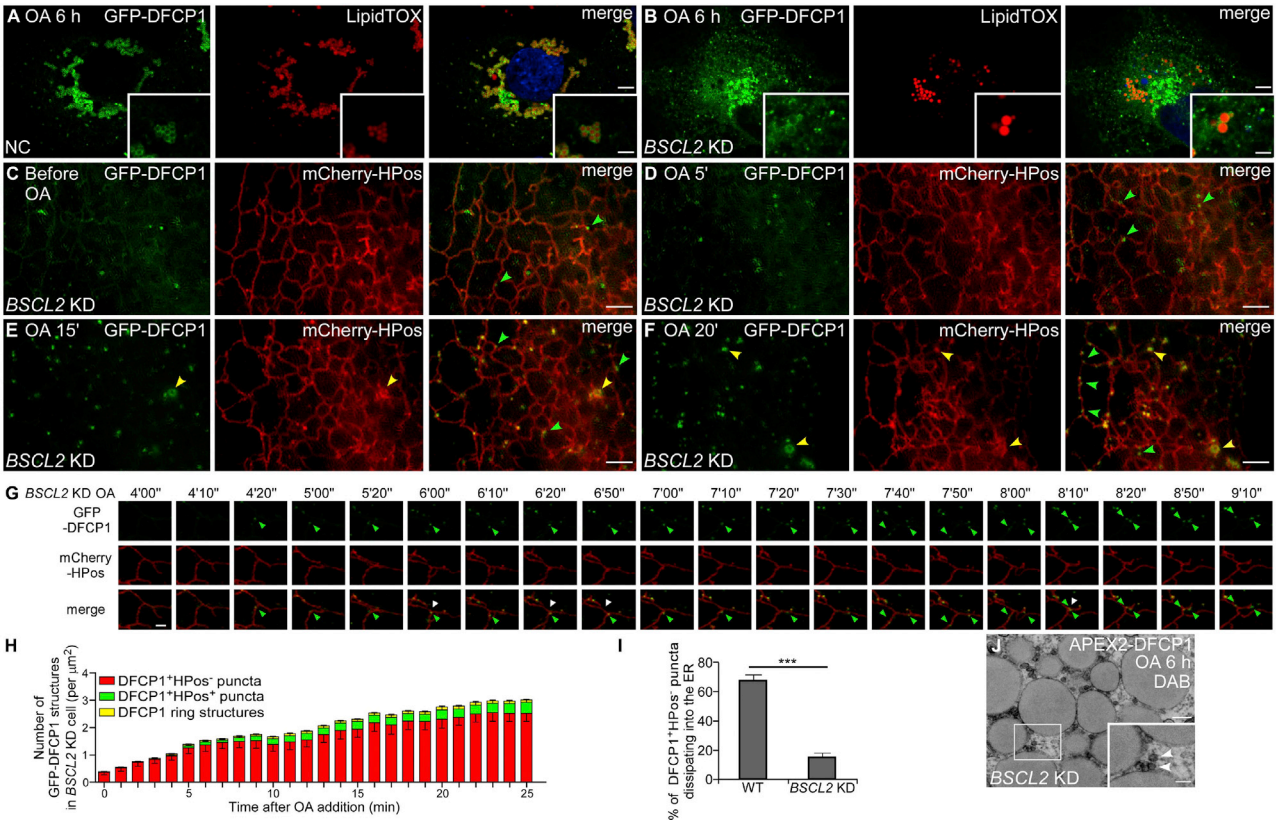

Figure 3. BSCL2 Regulates the Fusion of Nascent DFCP1 Puncta and the LD Localization of DFCP1

(A and B) After 6-h OA treatment, compared with NC cells (A), the localization of DFCP1 on LipidTOX-positive LDs is greatly suppressed and many punctate GFP-DFCP1 structures are present in *BSCL2* KD COS7 cells (B). Scale bars, 5 μm (inserts, 2 μm).

(C) GI-SIM images show that the ER localization of DFCP1 is weaker before OA addition in *BSCL2* KD cells. A few DFCP1^{+}HPos^{-} puncta (green arrows in the merge panel) are present on the ER.

(D–F) The formation of DFCP1 puncta at different time points after OA treatment in *BSCL2* KD cells. The number of DFCP1^{+}HPos^{-} puncta (green arrowheads) remains high from 5 min to 20 min (D–F). A few GFP-DFCP1 ring structures colocalize with mCherry-HPos in small or large LDs (yellow arrows in E and F). Scale bars, 2 μm (C–F).

(G) GI-SIM images at selected time points after OA addition showing the movement of nascent DFCP1 puncta in *BSCL2* KD cells. One DFCP1^{+}HPos^{-} punctum (green arrow) moves along the ER to the three-way junction site (white arrowhead), where it stays from 6′20″–6′50″ before moving away on the ER. Another DFCP1^{+}HPos^{-} punctum (OA 7′40″–9′10″, green arrowhead) moves along the ER and touches the first DFCP1 punctum (green arrowhead) at the ER three-way junction site. The two nascent DFCP1 puncta then separate onto different ER strands and do not fuse or grow in size. The ER three-way junction is a highly dynamic structure. Scale bar, 800 nm.

(H) Quantification of the number of DFCP1 structures in *BSCL2* KD cells (n = 13 areas of 10 μm^2 from 5 cells were examined for each time point). Data are shown as mean ± SEM.

(I) The percentage of DFCP1^{+}HPos^{-} puncta that dissipate into the ER within 25 min in wild-type and *BSCL2* KD cells (wild-type, n = 210 nascent DFCP1 puncta from 4 cells; *BSCL2* KD, n = 142 nascent DFCP1 puncta from 4 cells). Data are shown as mean ± SEM. ***p < 0.001.

(J) Cells expressing APEX2-DFCP1 shows that strong DAB-stained signals locate on nascent LDs (<100 nm), but not on small or supersized LDs (~300 nm and ~1 μm, respectively), in *BSCL2* KD cells. Arrowheads indicate DAB-stained structures. Scale bar, 200 nm (insert, 100 nm).

See also Figure S4.

DFCP1 Modulates the Formation of ER Contacts with LDs

After OA treatment for 6 h, the ER marker GFP-Sec61β was separable from LDs in control cells (Figure S5M) while they closely enveloped the LDs in DFCP1-overexpressing cells (Figure S5N). This suggests that the ER is closely associated with LDs. The mobility of LDs is affected by their association with the ER (Salo et al., 2016). We measured LD mobility after 1-h OA treatment and found that it was increased from 0.060 μm/s in control cells to 0.106 μm/s in *DFCP1* KD cells and reduced to 0.051 μm/s in DFCP1-overexpressing cells (Figures S5O–S5R). We also purified LDs to assess the association of ER with LDs. The ER-localized protein Sec61β dramatically accumulated in LDs purified from DFCP1-overexpressing cells compared to control cells (Figure 4H).

EM analysis was performed to directly visualize the contact between the ER and LDs. Compared to control cells, the percentage of LDs in contact with the ER, as well as their average perimeter, was decreased in *DFCP1* KD cells (Figures 4I–4L), while ER-LD contact was dramatically elevated in cells

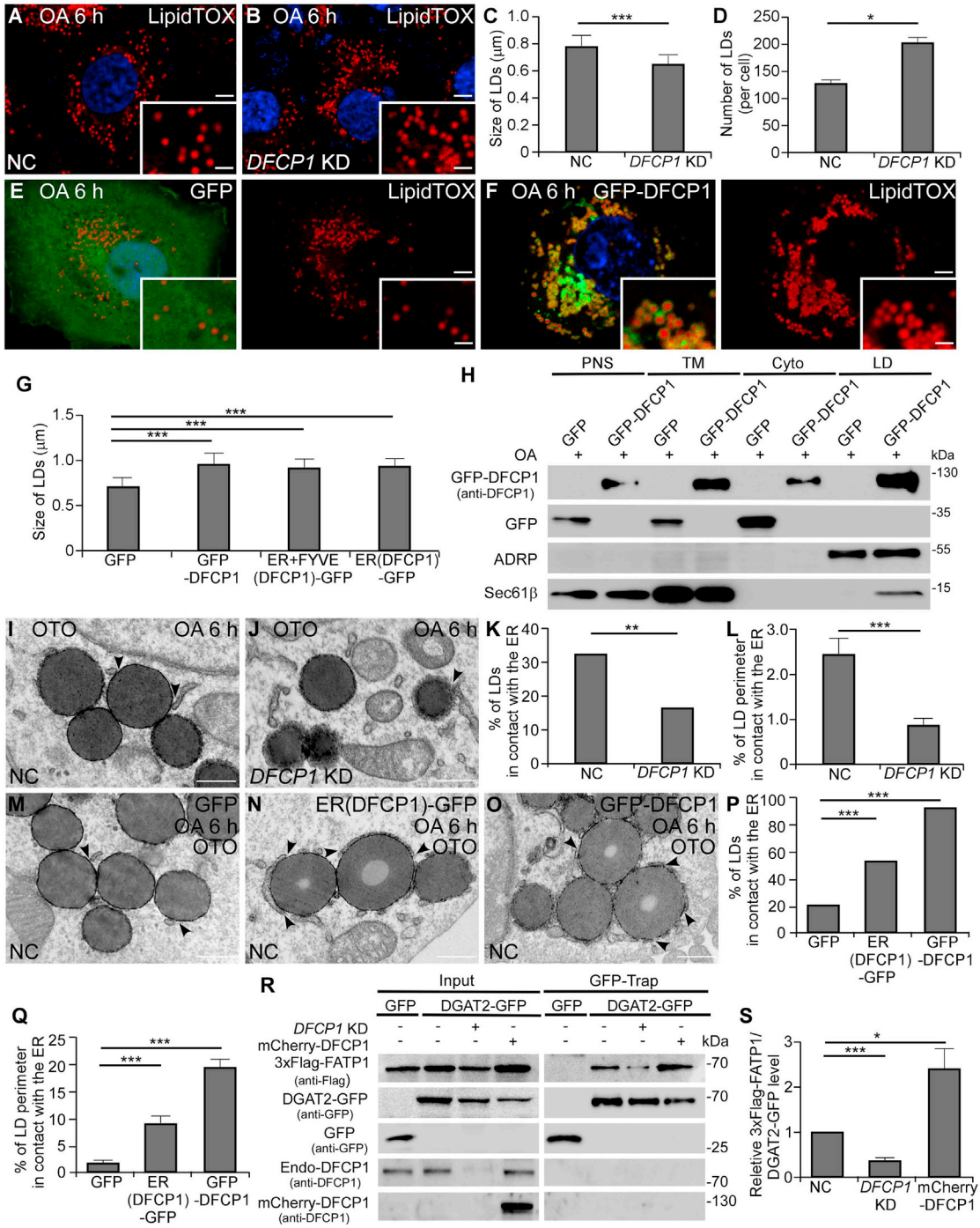

Figure 4. DFCP1 Regulates the Size of LDs and the Formation of ER-LD Contacts

(A and B) After 6-h OA treatment, *DFCP1* KD cells (B) contain more and smaller LDs than control (NC) cells (A). Scale bars, 5 μm (inserts, 2 μm).

(C) The size of LDs in NC and *DFCP1* KD COS7 cells (NC, n = 124 LDs from 7 cells; *DFCP1* KD, n = 200 LDs from 10 cells). Data are shown as mean ± SD. ***p < 0.001.

(D) The number of LDs per cell (NC, n = 7 cells; *DFCP1* KD, n = 10 cells) is quantified and shown as mean ± SEM. *p < 0.05.

(E–G) Overexpression of DFCP1 (F) increases the LD size in COS7 cells, compared with control cells (E). The structure near the nucleus that is strongly positive for GFP-DFCP1 but negative for LipidTOX is the Golgi apparatus. Quantification of the LD size in cells expressing GFP, GFP-DFCP1, ER+FYVE(DFCP1)-GFP, and ER(DFCP1)-GFP (n = 90, 102, 116, and 91 LDs, respectively) is shown in (G) as mean ± SD. Related to Figures S5G and S5H. ***p < 0.001. Scale bars, 5 μm (inserts, 2 μm).

(legend continued on next page)

overexpressing ER(DFCP1) or DFCP1 (Figures 4M–4Q). ER-LD contact was also decreased in *DFCP1* KD and increased in DFCP1-overexpressing HeLa cells (Figures S5S–S5W). Thus, DFCP1 promotes the formation of ER-LD contacts.

We next examined the formation of the FATP1-DGAT2 complex, which has been shown to tether the ER to LD contacts for LD expansion (Xu et al., 2012). Levels of FATP1 co-immunoprecipitated by DGAT2 were higher in DFCP1-overexpressing cells and lower in *DFCP1* KD cells (Figures 4R and 4S), supporting a role of DFCP1 in mediating ER-LD contact.

Rab18 Is Required for LD Targeting of DFCP1 and for the Role of DFCP1 in Mediating ER-LD Contact

Previous studies showed that upon LD induction, Rab18 localizes to LDs and induces close apposition of LDs with the ER (Ozeki et al., 2005). The LD localization of Rab18 depends on its activation (Ozeki et al., 2005). A GTPase-defective mutant (Q67L) of Rab18, but not a GDP-bound mutant (S22N), showed LD localization in COS7 cells (Figures S6A and S6B). DFCP1-RFP colocalized with GFP-Rab18(Q67L) on LDs after 6-h OA treatment (Figure S6C). Rab18 binds to the NAG-RINT-ZW10 (NRZ) tethering complex to modulate ER-LD contact in preadipocytes (Xu et al., 2018). mCherry-DFCP1 colocalized with GFP-Rab18 and 3 × Myc-ZW10 on LDs after 6-h OA treatment (Figure S6D). Knocking down *Rab18* and *ZW10* causes the formation of supersized LDs in 3T3-L1 preadipocytes (Figures S6E–S6I) (Xu et al., 2018). However, in *Rab18* or *ZW10* KD COS7 cells, the LDs were smaller and more abundant, similar to *DFCP1* KD COS7 cells (Figures S6J–S6Q). *DFCP1* KD caused the formation of supersized LDs in 3T3-L1 cells (Figures S6R and S6S). These results indicate that Rab18, ZW10, and DFCP1 play a similar role in LD biogenesis and that inactivation of these components causes different phenotypes in different cell types.

We used GI-SIM to examine whether Rab18 labels nascent LD structures. Rab18(Q67L), which exhibits strong LD localization, was used to facilitate the analysis. GFP-Rab18(Q67L) was distributed throughout the ER before OA addition (Figure 5A). After OA treatment, GFP-Rab18(Q67L) condensed at discrete sites on the ER that colocalized with mCherry-DFCP1 puncta and ring structures (Figures 5B and 5C; Video S4). GFP-Rab18(Q67L)-positive sites and mCherry-DFCP1 puncta emerged from the ER at the same time, and the two markers moved together (Figure 5D; Video S4), indicating that Rab18 is also targeted to nascent LDs. In *BSCL2* KD COS7 cells, Rab18 formed numerous puncta that failed to be stained by LipidTOX (Figures 5E and 5F). GI-SIM analysis revealed that Rab18 formed punctate structures that colocalized with nascent DFCP1 puncta in *BSCL2* KD cells after OA treatment (Figures S6T and S6U; Video S5).

We next examined whether Rab18 regulates the LD localization of DFCP1 upon LD induction. In *Rab18* KD cells, GFP-DFCP1 failed to enclose LDs after 6-h OA treatment (Figure 5G). GI-SIM showed that formation of nascent DFCP1 puncta was also suppressed in *Rab18* KD cells after OA treatment (Figure S7A). Consistent with this, EM analysis revealed that LDs in *Rab18* KD cells were not labeled by APEX2-DFCP1 (Figures S7B and S7C). *Rab18* depletion also suppressed the ER-LD contacts induced by DFCP1 overexpression. The percentage of LDs, as well as the average perimeter, in contact with the ER in cells overexpressing GFP-DFCP1 was decreased by simultaneous depletion of *Rab18* (Figures 5H–5K). *ZW10* KD did not affect the LD localization of DFCP1 (Figure S7D). These results indicate that Rab18 is required for the LD localization of DFCP1 and for its function in tethering the ER to LDs.

GFP-Rab18 was still targeted to LDs in *DFCP1* KD cells (Figure S7E), but at a reduced level. The percentage of LDs and the average perimeter in contact with the ER in cells overexpressing Rab18, however, were decreased by *DFCP1* KD (Figures 5L–5P). Therefore, DFCP1 is also required for Rab18-mediated ER-LD contact.

DFCP1 Forms a Complex with Rab18-ZW10

We determined whether DFCP1 is directly recruited to LDs by Rab18. GFP-DFCP1 precipitated endogenous Rab18 in co-immunoprecipitation (coIP) assays (Figure 6A). Levels of precipitated Rab18 were slightly increased after OA treatment (Figure 6A). Endogenous DFCP1 was also co-immunoprecipitated by endogenous Rab18 (Figure 6B). Compared to wild-type Rab18, the levels of DFCP1 co-precipitated by Rab18(Q67L) and Rab18(S22N) were more and less, respectively, after 6-h OA treatment (Figure 6C). *In vitro* pull-down assays showed that DFCP1 directly bound to Rab18 and Rab18(Q67L), but not to GST-Rab18(S22N) (Figures 6D and S7F). The N terminus and also the ER localization domain of DFCP1 exhibited Rab18-binding activity in *in vitro* GST pull-down assays

(H) GFP-DFCP1 is enriched in the LD fraction. Levels of the ER membrane (detected by Sec61β) cofractionated with LDs is increased in GFP-DFCP1 overexpression cells. PNS, post-nuclear supernatant; TM, total membrane; Cyto, cytosol; LD, lipid droplets. ADRP, LD marker; Sec61β, ER marker.

(I and J) EM images showing ER-LD contacts in NC (I) and *DFCP1* KD (J) cells. Arrowheads indicate ER-LD contact sites. Osmium-thiocarbohydrazied-osmium (OTO) staining was used to enhance the contrast of lipid-containing membranes and droplets. Images showing LDs stained with OTO are indicated. Scale bars, 500 nm.

(K and L) The percentage of LDs displaying contacts with the ER (contacts with a length ≥ 0.02 μm were examined in this study) (K) and the percentage of the LD perimeter (for LDs contacting the ER) in contact with the ER (L) in NC and *DFCP1* KD cells (n = 117 and 132 LDs, respectively). Mean ± SEM is shown. ***p < 0.001; **p < 0.01.

(M–O) EM images showing ER-LD contacts in cells overexpressing GFP (M), ER(DFCP1)-GFP (N), and GFP-DFCP1 (O). Arrowheads indicate the extensive ER-LD contact sites. Scale bars, 500 nm.

(P and Q) The percentage of LDs in contact with the ER (P) and the percentage of the LD perimeter in contact with the ER (Q) in NC cells expressing GFP, ER(DFCP1)-GFP, and GFP-DFCP1 (n = 92, 103 and 103 LDs, respectively). Mean ± SEM is shown. ***p < 0.001.

(R and S) A GFP-Trap assay shows that the level of 3 × FLAG-FATP1 co-immunoprecipitated by DGAT2-GFP is higher in DFCP1-overexpressing cells but lower in *DFCP1* KD cells (R). Quantifications of 3 × FLAG-FATP1 (normalized by DGAT2-GFP) precipitated by DGAT2 are shown in (S) as mean ± SEM (n = 3 individual experiments). *p < 0.05; ***p < 0.001.

See also Figure S5.

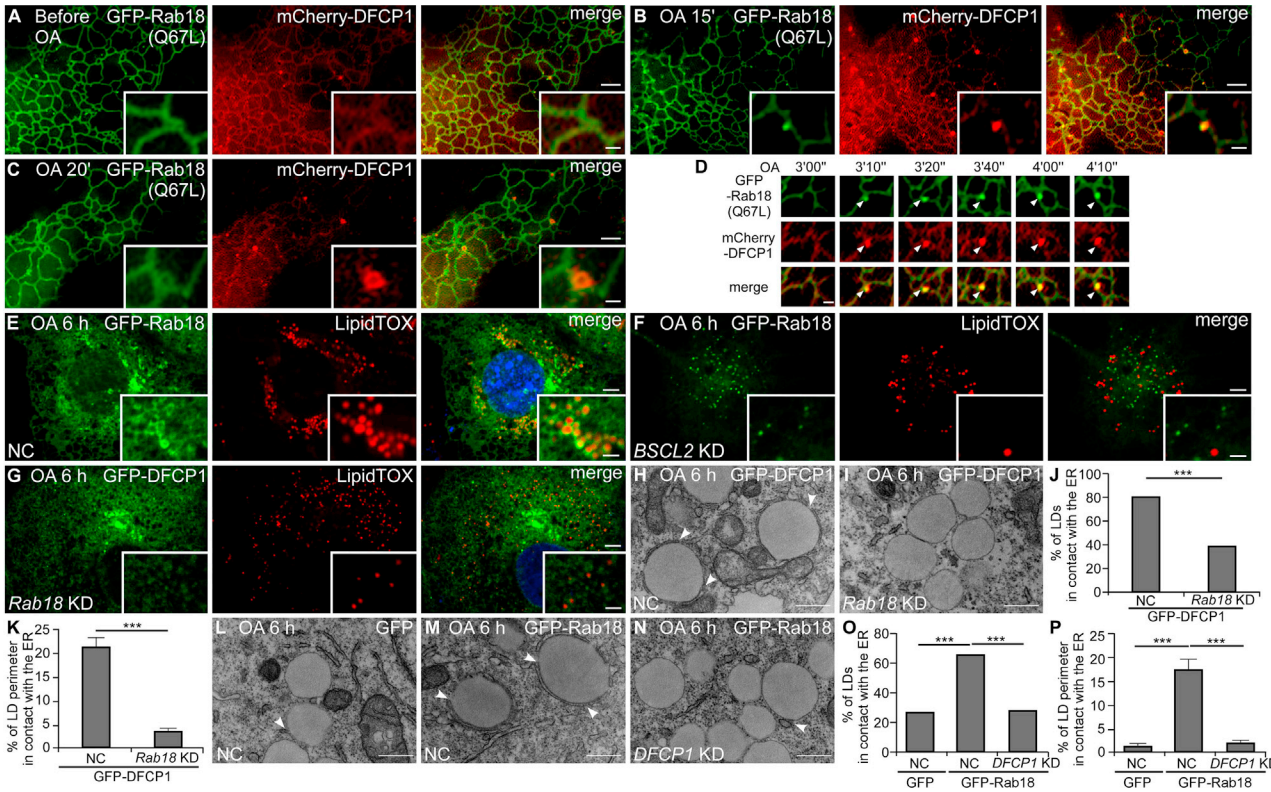

Figure 5. Rab18 Is Required for LD Targeting of DFCP1 and for the Role of DFCP1 in Mediating the ER-LD Contact

(A–C) GI-SIM shows that GFP-Rab18(Q67L) colocalizes with mCherry-DFCP1 on the ER before OA addition (A). GFP-Rab18(Q67L) forms discrete sites on the ER that colocalize with mCherry-DFCP1 puncta and ring structures after OA treatment for 15 min (B) and 20 min (C). Scale bars, 2 μm; inserts, 400 nm.

(D) GI-SIM images at a series of time points after OA treatment shows that mCherry-DFCP1 puncta and GFP-Rab18(Q67L)-positive sites (arrowheads) emerge from the ER at the same time and move together. Scale bar, 400 nm.

(E and F) After 6-h OA treatment, Rab18 encloses LDs in NC cells (E). In *BSCL2* KD cells, Rab18 fails to localize to LipidTOX-positive LDs and form numerous punctate structures (F).

(G) After 6-h OA treatment, GFP-DFCP1 fails to move to LDs in *Rab18* KD cells.

(E–G) Scale bars, 5 μm (inserts, 2 μm).

(H and I) ER-LD contacts (arrowheads) are greatly enhanced in DFCP1-overexpressing cells (H) and reduced by simultaneous depletion of *Rab18* (I). LDs are not stained with OTO in these experiments. Scale bars, 500 nm.

(J and K) Quantification of the percentage of LDs in contact with the ER (J) and the percentage of the LD perimeter in contact with the ER (K) (GFP-DFCP1, n = 106 LDs; *Rab18* KD GFP-DFCP1, n = 102 LDs). Mean ± SEM is shown. ***$p < 0.001$.

(L–N) EM analysis of the ER-LD contact in NC cells (L), Rab18-overexpressing cells (M), and Rab18-overexpressing cells with simultaneous *DFCP1* depletion (N). Scale bars, 500 nm.

(O and P) The percentage of LDs in contact with the ER (O) and the percentage of the LD perimeter in contact with the ER (P) (GFP, n = 106 LDs; GFP-Rab18, n = 102 LDs; *DFCP1* KD GFP-Rab18, n = 109 LDs). Mean ± SEM is shown. ***$p < 0.001$.

See also Figures S6 and S7.

(Figure S7G). These results suggest that DFCP1 acts as a Rab18 effector.

Endogenous ZW10 was also co-immunoprecipitated by GFP-DFCP1, and levels of precipitated ZW10 were increased after OA treatment (Figure 6A). The interaction between Rab18 and ZW10 was reduced in *DFCP1* KD cells (Figure 6E). Knocking down Rab18 and ZW10 had no obvious effect on the DFCP1-ZW10 interaction and the DFCP1-Rab18 interaction, respectively (Figures 6F and S7H). Depletion of one component of the Rab18-DFCP1-ZW10 complex reduced the levels of the other proteins (Figure 6G). The ER-localized transmembrane protein EPG-3 (VMP1) modulates the stability of ER-LD contacts (Zhao et al., 2017). In *VMP1* KO cells, the ER-LD contacts are dramatically increased (Zhao et al., 2017). We found that compared to control cells, interactions of DFCP1 with Rab18 and ZW10 were increased in *VMP1* KO cells (Figure 6H). Therefore, DFCP1 forms a complex with Rab18-ZW10 and modulates the assembly and/or stability of the complex.

BSCL2 Modulates ER-LD Contact Mediated by the DFCP1-Rab18-ZW10 Complex

BSCL2 has been shown to modulate the formation, stabilization, and function of ER-LD contacts (Salo et al., 2016). We determined whether BSCL2 regulates ER-LD contacts mediated by the Rab18-DFCP1 complex. Simultaneous depletion of *BSCL2* resulted in the formation of both small and supersized LDs in

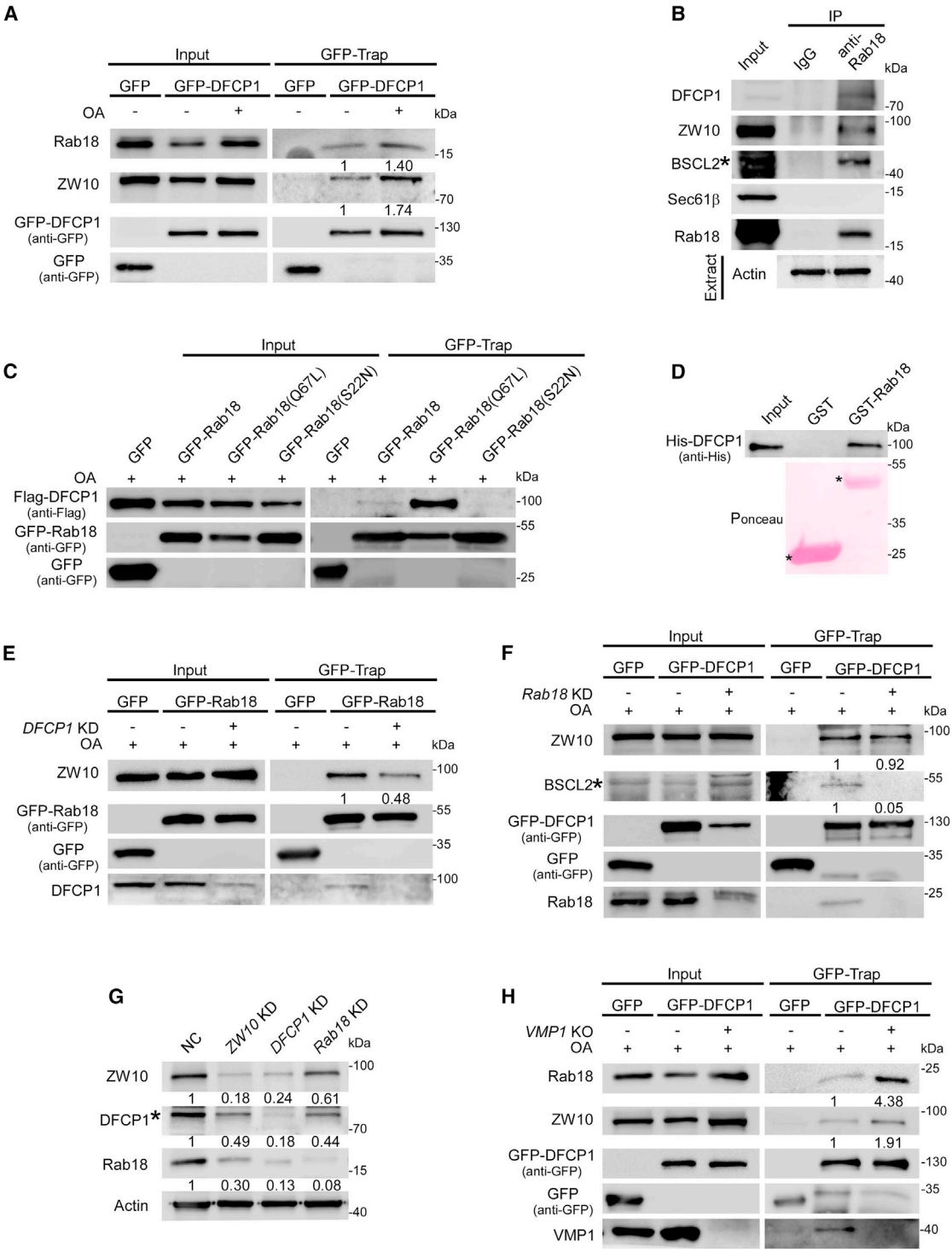

Figure 6. DFCP1 Interacts with the Rab18-ZW10 Tethering Complex

(A) A GFP-Trap assay shows that GFP-DFCP1 precipitates endogenous Rab18 and ZW10. Levels of Rab18 and ZW10 (normalized by GFP-DFCP1 levels) are quantified.

(B) A coIP assay shows that endogenous Rab18 precipitates endogenous DFCP1, ZW10 and BSCL2. Asterisk (*) indicates the band corresponding to BSCL2.

(C) A GFP-Trap assay shows that DFCP1 is co-immunoprecipitated by Rab18(Q67L), but not by Rab18(S22N), after 6-h OA treatment. Wild-type Rab18 also weakly precipitates DFCP1 in the same assay.

(D) An *in vitro* pull-down assay shows that DFCP1 directly binds to Rab18. Asterisk (*) indicates the target band.

(legend continued on next page)

DFCP1- or *Rab18*-depleted or overexpressing cells (Figures S7I and S7J; data not shown). Consistent with previous studies (Salo et al., 2016), association of the ER with the LD surface was increased on average in *BSCL2* KD cells compared to control cells (Figures 7A, 7B, 7E, and 7F). Enhanced ER-LD contact in DFCP1-overexpressing cells was suppressed by simultaneous depletion of *BSCL2*, so that the extent of ER-LD contact resembled that in *BSCL2* single KD cells (Figures 7C–7F).

We examined whether BSCL2 interacts with the DFCP1-Rab18 complex. In coIP assays, endogenous Rab18 precipitated endogenous BSCL2 (Figure 6B). BSCL2 was also co-immunoprecipitated by DFCP1 (Figure 6F). The ER domain of DFCP1 precipitated BSCL2 in coIP assays (Figure S7K). The interaction between DFCP1 and BSCL2 was not affected by OA treatment (Figure S7L) but was greatly suppressed in *Rab18* KD cells (Figure 6F), suggesting that Rab18 facilitates the interaction between BSCL2 and DFCP1. The interaction of Rab18 with BSCL2 was not reduced in *ZW10* KD cells (Figure S7H). Levels of endogenous Rab18 and ZW10 co-precipitated by DFCP1 were not evidently affected by *BSCL2* depletion (Figure S7M). These results suggested that BSCL2 interacts with the Rab18-DFCP1-ZW10 complex to modulate ER-LD contact formation. Depletion of *Rab18* or *DFCP1* also suppressed the increased ER-LD contact in *BSCL2* KD cells (Figures 7G–7N), indicating that the DFCP1-Rab18 complex also modulates ER-LD contact independent of BSCL2.

DISCUSSION

Fusion of DFCP1-Labeled Nascent LD Structures at the Early Stages of LD Biogenesis

LDs are generated from the ER (Walther et al., 2017; Qi et al., 2017). Neutral lipids synthesized in the ER membrane bilayer accumulate into lens-like structures, which further grow and bud into the cytoplasm. These newly budded nascent LDs do not contain enough lipids to be detected by neutral lipid dyes (e.g., BODIPY and LipidTOX) but can be labeled by HPos and LiveDrop (Kassan et al., 2013; Wang et al., 2016). The nascent LDs reassociate with the ER to acquire more lipids and/or TG synthesis enzymes (e.g., GPAT4 and DGAT2) to generate TG for LD growth (Wang et al., 2016; Salo et al., 2016).

Using super-resolution GI-SIM, which has a much higher speed and greater imaging depth than confocal microscopy (Nixon-Abell et al., 2016), we visualized the dynamics of early steps involved in LD formation. Upon LD induction, small DFCP1 puncta emerge from the ER, and the formation of these puncta depends on TG synthesis. DFCP1 puncta appear earlier and are more abundant than puncta labeled by HPos and LiveDrop. Formation of DFCP1-labeled nascent structures is reversible, and the majority of them dissipate into the ER. The DFCP1-labeled puncta move along the ER, fuse with each other, and mature into more advanced LD structures that are positive for both HPos and DFCP1. The double-positive puncta are mainly located at ER three-way junctions and further grow into mature LDs (Figure 7O). Thus, formation of DFCP1-positive nascent structures constitutes an early step of LD formation. How DFCP1 concentrates at discrete sites upon LD induction remains unresolved, as does the nature of DFCP1 puncta. Nascent DFCP1 structures may be enriched in TGs. Alternatively, DFCP1 may accumulate at ER sites with a membrane change associated with LD formation.

In *BSCL2* KD cells, the dissipation of DFCP1 puncta into the ER and fusion of nascent LDs and their maturation into expanding LDs at three-way junctions is greatly inhibited. The mechanism by which BSCL2 controls the dynamics of DFCP1 puncta at early stages of LD biogenesis has yet to be determined. BSCL2 could mediate the reengagement of nascent LDs with the ER and/or stabilize them on the ER by interacting with the DFCP1-Rab18 complex and other unidentified factors. Another possibility is that BSCL2 may modulate the lipid and protein composition of nascent DFCP1 structures to specify their fusion capability.

DFCP1 Forms a Complex with Rab18-ZW10 to Mediate ER-LD Contact

Targeting DFCP1 to nascent and mature LDs requires Rab18. DFCP1 acts as a Rab18 effector. DFCP1 binds strongly to active mutant Rab18(Q67L), but not to GDP-bound mutant Rab18(S22N). Rab18 directly interacts with ZW10, which further interacts with ER-localized SNAREs to establish ER-LD contact (Xu et al., 2018). DFCP1 mediates the ER-LD contact by forming a complex with Rab18 and ZW10. The number of LDs and also the average length of the LD perimeter in contact with the ER is increased by overexpression of DFCP1 and reduced by depletion of DFCP1. The enhanced ER-LD contact caused by DFCP1 overexpression depends on Rab18, and the enhanced ER-LD contact induced by Rab18 overexpression requires DFCP1. In *VMP1*/*EPG-3*-depleted cells, in which ER-LD contact is greatly enhanced (Zhao et al., 2017), the formation of the DFCP1-Rab18-ZW10 complex is elevated. LD biogenesis is modulated by ER-LD contact. The LDs are smaller and more numerous in *DFCP1* KD COS7 and HeLa cells and larger in cells overexpressing DFCP1. In *Rab18* or *ZW10* KD COS7 and HeLa cells, LDs are also smaller and greater in number. Formation of the FATP1-DGAT2 complex at ER-LD contact sites for TG synthesis is reduced by *DFCP1* depletion and enhanced by DFCP1

(E) The interaction between Rab18 and ZW10 is reduced in *DFCP1* KD cells. Levels of ZW10 co-precipitated by GFP-Rab18 (normalized by GFP-Rab18 levels) are quantified.

(F) Endogenous ZW10 and BSCL2 proteins are co-immunoprecipitated by GFP-DFCP1. Levels of BSCL2 and ZW10 (normalized by GFP-DFCP1 levels) are quantified. Asterisk (*) indicates the band corresponding to BSCL2.

(G) Knocking down *Rab18*, *DFCP1*, and *ZW10* reduces the levels of other proteins. Levels of Rab18, DFCP1, and ZW10 (normalized by Actin levels) are quantified. Asterisk (*) indicates the band corresponding to DFCP1.

(H) Levels of endogenous Rab18 and ZW10 co-immunoprecipitated by GFP-DFCP1 are enhanced in *VMP1* knockout (KO) cells. Levels of Rab18 and ZW10 (normalized by GFP-DFCP1 levels) are quantified.

See also Figure S7.

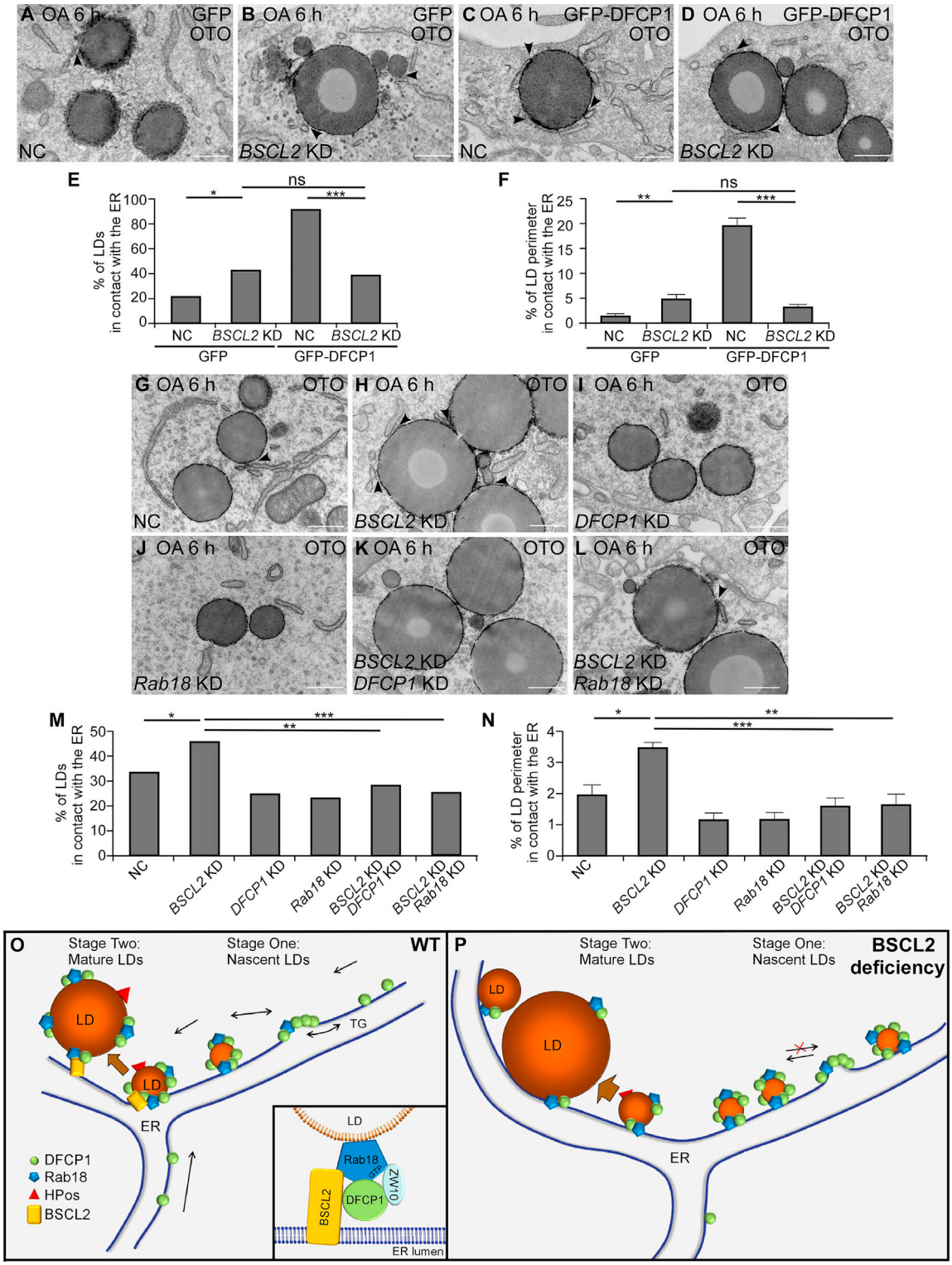

Figure 7. BSCL2 Modulates ER-LD Contact Mediated by the Rab18-DFCP1 Complex

(A–D) EM analysis of ER-LD contact in NC cells (A), *BSCL2* KD cells (B), DFCP1-overexpressing cells (C), and DFCP1-overexpressing cells with simultaneous *BSCL2* depletion (D). The ER-LD contact site is indicated by arrowheads. Scale bars, 500 nm.

(legend continued on next page)

overexpression (Xu et al., 2012). The DFCP1-Rab18-ZW10 complex may also interact with lipid transfer proteins or regulate other aspects of LDs such as lipid and protein composition to modulate LD biogenesis.

Two types of ER-LD contact have been reported that act differently in lipid and protein transfer. One type involves close apposition of the ER to LDs. Formation of these contacts is mediated by protein-protein and/or protein-phosphoinositide interactions (Phillips and Voeltz, 2016). Another type of contact contains membrane extensions linking the ER to LDs. Neutral lipids generated in the ER and ER-localized TG synthesis enzymes are directly transferred via these extensions to LDs. LDs in different cell types have unique features such as lipid composition and LD proteins. For example, phospholipid metabolism may be distinct and the LD fusion-promoting protein Fsp27 may be differentially expressed in different cell types (Gong et al., 2011; Qi et al., 2017). Formation of these two types of ER-LD contact may be differentially modulated by the DFCP1-Rab18-ZW10 complex in different cell types. In 3T3-L1 cells, depletion of components of the DFCP1-Rab18-ZW10 complex leads to formation of supersized LDs, which could be caused by the formation of membrane extensions between the ER and LDs (Wolinski et al., 2015).

BSCL2 Regulates the Role of the DFCP1-Rab18-ZW10 Complex in ER-LD Contact Formation

BSCL2 forms distinct puncta at ER-LD contact sites and modulates the formation, stabilization, and function of ER-LD contacts (Wang et al., 2016; Salo et al., 2016; Cartwright et al., 2015). BSCL2 has been shown to facilitate the transport of proteins such as ACSL3 and HPos from the ER into expanding LDs and/or to prevent equilibration of ER and LD surface components (Wang et al., 2016; Salo et al., 2016). We found that in the absence of *BSCL2*, trafficking of DFCP1 and Rab18 to nascent LD structures occurs, while their localization to mature LDs is greatly reduced, which may result from their impaired transfer from the ER to expanding LDs or retention at the LD monolayer. Depletion of *BSCL2* suppresses the enhanced ER-LD contact in DFCP1- or Rab18-overexpressing cells. BSCL2 may directly participate in contact formation by interacting with the DFCP1-Rab18 complex. It is also possible that BSCL2 modulates the lipid and protein composition at the contact sites, which in turn facilitates the ER-LD contact mediated by the DFCP1-Rab18 complex. In *BSCL2* KO cells, ER-LD contacts are heterogeneous and irregular. A fraction of LDs, including supersized LDs, exhibit extensive contact and membrane bridges with the ER (Salo et al., 2016). The enhanced ER-LD contact in *BSCL2* KD cells is suppressed by simultaneous depletion of *Rab18* or *DFCP1*. Thus, the DFCP1-Rab18 complex has a BSCL2-independent function in tethering the ER with LDs.

The LD defect in *DFCP1*- and *Rab18*-depleted COS7 and HeLa cells is not identical to that in *BSCL2* KD cells. *DFCP1* KD and *Rab18* KD cells contain uniformly small LDs that are stained by lipid dyes. The LDs in *BSCL2* KD cells are heterogeneous in size and include the supersized LDs that may result from premature targeting of lipid synthesis enzymes and/or LD coalescence due to changes in phospholipid composition (Wang et al., 2016; Salo et al., 2016; Wolinski et al., 2015). BSCL2 appears to have other functions in the control of LD biogenesis in addition to mediating ER-LD membrane contact. Our study shows that the DFCP1-Rab18 complex is involved in modulating the formation and/or stability of ER-LD contacts to regulate LD biogenesis.

STAR★METHODS

Detailed methods are provided in the online version of this paper and include the following:

- KEY RESOURCES TABLE
- CONTACT FOR REAGENT AND RESOURCE SHARING
- EXPERIMENTAL MODEL AND SUBJECT DETAILS
  - Cell culture
- METHOD DETAILS
  - Plasmids
  - Transfection and RNA interference
  - Lipid droplet staining assay
  - Membrane fractions
  - LD mobility
  - LD purification
  - Co-immunoprecipitation assays
  - Protein expression and purification
  - *In vitro* pulldown assays
  - Electron microscopy
  - 3D-structured illumination microscopy

(E and F) The percentage of LDs in contact with the ER (E) and the percentage of the LD perimeter in contact with the ER (F) (NC, n = 92 LDs; *BSCL2* KD, n = 158 LDs; GFP-DFCP1, n = 103 LDs; *BSCL2* KD GFP-DFCP1, n = 139 LDs). Mean ± SEM is shown. ***p < 0.001; **p < 0.01; *p < 0.05; ns, not significant. Data for cells expressing GFP and GFP-DFCP1 are from Figures 4P and 4Q. These experiments were performed at the same time.
(G–L) EM analysis of ER-LD contact in NC cells (G), *BSCL2* KD cells (H), *DFCP1* KD cells (I), *Rab18* KD cells (J), and *DFCP1* KD cells with simultaneous *BSCL2* depletion (K) and *Rab18* KD cells with simultaneous *BSCL2* depletion (L). Arrowheads indicate ER-LD contact sites. Scale bars, 500 nm.
(M and N) Quantification of the percentage of LDs in contact with the ER (M) and the percentage of the LD perimeter in contact with the ER (N) (NC, n = 103 LDs; *BSCL2* KD, n = 155 LDs; *DFCP1* KD, n = 102 LDs; *Rab18* KD, n = 114 LDs; *DFCP1* KD with simultaneous KD *BSCL2*, n = 129 LDs; *Rab18* KD with simultaneous KD *BSCL2*, n = 132 LDs). Mean ± SEM is shown. ***p < 0.001; **p < 0.01; *p < 0.05
(O and P) Models for the initial stage of LD formation in control and *BSCL2*-deficient cells. Upon LD induction, DFCP1 associates with nascent LD structures in a manner that depends on TG synthesis. These nascent LDs move along the ER and fuse with each other at the ER three-way junction site to form expanding LDs. The nascent LDs may have detached from the ER or remain connected with the ER via thin membrane bridges. The nascent LDs can also dissipate into the ER. HPos mainly labels the expanding LD at ER three-way junction sites. BSCL2 modulates the dynamics and maturation of nascent LDs (stage one). As the expanding LDs grow in size, DFCP1 and Rab18 are also transported from the ER to the LD (stage two). The insert in (O) shows the formation of the DFCP1-Rab18-ZW10 complex at the ER-LD contact site. In *BSCL2*-deficient cells, dissipation of nascent DFCP1 puncta into the ER is inhibited. A few LDs engage with the ER for growth (P).
See also Figure S7.

- Immunoelectron microscopy
- FRAP experiment
- Grazing incidence SIM

- QUANTIFICATION AND STATISTICAL ANALYSIS

SUPPLEMENTAL INFORMATION

Supplemental Information can be found online at https://doi.org/10.1016/j.celrep.2019.03.025.

ACKNOWLEDGMENTS

We are grateful to Dr. Isabel Hanson for editing work. We would like to thank Dr. Shuoguo Li from the Center for Biological Imaging (CBI), Institute of Biophysics, for her help in taking and analyzing SIM images. This work was supported by grants to H.Z. from the Beijing Municipal Science and Technology Committee (Z181100001318003), NSFC (31630048, 31790403, 31421002, and 31561143001), the Strategic Priority Research Program of the Chinese Academy of Sciences (CAS) (XDB19000000), and the Key Research Program of Frontier Sciences, CAS (QYZDY-SSW-SMC006). The research is also partly supported by Fountain-Valley Life Sciences Fund of the University of Chinese Academy of Sciences Education Foundation.

AUTHOR CONTRIBUTIONS

Dong Li, P.S.L., and H.Z. designed the experiments. Dongfang Li, Y.G.Z., Di Li, H. Zhao, J.H., G.M., and D.F. performed the experiments. H. Zhao analyzed the EM images, and D.F. analyzed the immuno-EM images. Dong Li, Y.G.Z., and H. Zhang wrote the manuscript.

DECLARATION OF INTERESTS

The authors declare no competing interests.

Received: February 20, 2018
Revised: October 29, 2018
Accepted: March 7, 2019
Published: April 9, 2019

REFERENCES

Axe, E.L., Walker, S.A., Manifava, M., Chandra, P., Roderick, H.L., Habermann, A., Griffiths, G., and Ktistakis, N.T. (2008). Autophagosome formation from membrane compartments enriched in phosphatidylinositol 3-phosphate and dynamically connected to the endoplasmic reticulum. J. Cell Biol. *182*, 685–701.

Ben M'barek, K., Ajjaji, D., Chorlay, A., Vanni, S., Forêt, L., and Thiam, A.R. (2017). ER membrane phospholipids and surface tension control cellular lipid droplet formation. Dev. Cell *41*, 591–604.e7.

Bersuker, K., Peterson, C.W.H., To, M., Sahl, S.J., Savikhin, V., Grossman, E.A., Nomura, D.K., and Olzmann, J.A. (2018). A proximity labeling strategy provides insights into the composition and dynamics of lipid droplet proteomes. Dev. Cell *44*, 97–112.e7.

Cartwright, B.R., Binns, D.D., Hilton, C.L., Han, S., Gao, Q., and Goodman, J.M. (2015). Seipin performs dissectible functions in promoting lipid droplet biogenesis and regulating droplet morphology. Mol. Biol. Cell *26*, 726–739.

Choudhary, V., Ojha, N., Golden, A., and Prinz, W.A. (2015). A conserved family of proteins facilitates nascent lipid droplet budding from the ER. J. Cell Biol. *211*, 261–271.

Choudhary, V., Golani, G., Joshi, A.S., Cottier, S., Schneiter, R., Prinz, W.A., and Kozlov, M.M. (2018). Architecture of lipid droplets in endoplasmic reticulum is determined by phospholipid intrinsic curvature. Curr. Biol. *28*, 915–926.e9.

Fei, W., Shui, G., Zhang, Y., Krahmer, N., Ferguson, C., Kapterian, T.S., Lin, R.C., Dawes, I.W., Brown, A.J., Li, P., et al. (2011). A role for phosphatidic acid in the formation of "supersized" lipid droplets. PLoS Genet. *7*, e1002201.

Gong, J., Sun, Z., Wu, L., Xu, W., Schieber, N., Xu, D., Shui, G., Yang, H., Parton, R.G., and Li, P. (2011). Fsp27 promotes lipid droplet growth by lipid exchange and transfer at lipid droplet contact sites. J. Cell Biol. *195*, 953–963.

Itakura, E., and Mizushima, N. (2010). Characterization of autophagosome formation site by a hierarchical analysis of mammalian Atg proteins. Autophagy *6*, 764–776.

Joshi, A.S., Zhang, H., and Prinz, W.A. (2017). Organelle biogenesis in the endoplasmic reticulum. Nat. Cell Biol. *19*, 876–882.

Kassan, A., Herms, A., Fernández-Vidal, A., Bosch, M., Schieber, N.L., Reddy, B.J., Fajardo, A., Gelabert-Baldrich, M., Tebar, F., Enrich, C., et al. (2013). Acyl-CoA synthetase 3 promotes lipid droplet biogenesis in ER microdomains. J. Cell Biol. *203*, 985–1001.

Kory, N., Farese, R.V., Jr., and Walther, T.C. (2016). Targeting fat: mechanisms of protein localization to lipid droplets. Trends Cell Biol. *26*, 535–546.

Krahmer, N., Guo, Y., Wilfling, F., Hilger, M., Lingrell, S., Heger, K., Newman, H.W., Schmidt-Supprian, M., Vance, D.E., Mann, M., et al. (2011). Phosphatidylcholine synthesis for lipid droplet expansion is mediated by localized activation of CTP:phosphocholine cytidylyltransferase. Cell Metab. *14*, 504–515.

Lam, S.S., Martell, J.D., Kamer, K.J., Deerinck, T.J., Ellisman, M.H., Mootha, V.K., and Ting, A.Y. (2015). Directed evolution of APEX2 for electron microscopy and proximity labeling. Nat. Methods *12*, 51–54.

Nixon-Abell, J., Obara, C.J., Weigel, A.V., Li, D., Legant, W.R., Xu, C.S., Pasolli, H.A., Harvey, K., Hess, H.F., Betzig, E., et al. (2016). Increased spatiotemporal resolution reveals highly dynamic dense tubular matrices in the peripheral ER. Science *354*, aaf3928.

Ozeki, S., Cheng, J., Tauchi-Sato, K., Hatano, N., Taniguchi, H., and Fujimoto, T. (2005). Rab18 localizes to lipid droplets and induces their close apposition to the endoplasmic reticulum-derived membrane. J. Cell Sci. *118*, 2601–2611.

Phillips, M.J., and Voeltz, G.K. (2016). Structure and function of ER membrane contact sites with other organelles. Nat. Rev. Mol. Cell Biol. *17*, 69–82.

Qi, Y., Sun, L., and Yang, H. (2017). Lipid droplet growth and adipocyte development: mechanistically distinct processes connected by phospholipids. Biochim Biophys Acta Mol Cell Biol Lipids *1862* (*10 Pt B*), 1273–1283.

Salo, V.T., Belevich, I., Li, S., Karhinen, L., Vihinen, H., Vigouroux, C., Magré, J., Thiele, C., Hölttä-Vuori, M., Jokitalo, E., and Ikonen, E. (2016). Seipin regulates ER-lipid droplet contacts and cargo delivery. EMBO J. *35*, 2699–2716.

Thiam, A.R., Antonny, B., Wang, J., Delacotte, J., Wilfling, F., Walther, T.C., Beck, R., Rothman, J.E., and Pincet, F. (2013). COPI buds 60-nm lipid droplets from reconstituted water-phospholipid-triacylglyceride interfaces, suggesting a tension clamp function. Proc. Natl. Acad. Sci. USA *110*, 13244–13249.

Walther, T.C., Chung, J., and Farese, R.V., Jr. (2017). Lipid droplet biogenesis. Annu. Rev. Cell Dev. Biol. *33*, 491–510.

Wang, H., Becuwe, M., Housden, B.E., Chitraju, C., Porras, A.J., Graham, M.M., Liu, X.N., Thiam, A.R., Savage, D.B., Agarwal, A.K., et al. (2016). Seipin is required for converting nascent to mature lipid droplets. eLife *5*, e16582.

Wilfling, F., Wang, H., Haas, J.T., Krahmer, N., Gould, T.J., Uchida, A., Cheng, J.X., Graham, M., Christiano, R., Fröhlich, F., et al. (2013). Triacylglycerol synthesis enzymes mediate lipid droplet growth by relocalizing from the ER to lipid droplets. Dev. Cell *24*, 384–399.

Wilfling, F., Thiam, A.R., Olarte, M.J., Wang, J., Beck, R., Gould, T.J., Allgeyer, E.S., Pincet, F., Bewersdorf, J., Farese, R.V., Jr., and Walther, T.C. (2014). Arf1/COPI machinery acts directly on lipid droplets and enables their connection to the ER for protein targeting. eLife *3*, e01607.

Wolinski, H., Hofbauer, H.F., Hellauer, K., Cristobal-Sarramian, A., Kolb, D., Radulovic, M., Knittelfelder, O.L., Rechberger, G.N., and Kohlwein, S.D. (2015). Seipin is involved in the regulation of phosphatidic acid metabolism at a subdomain of the nuclear envelope in yeast. Biochim. Biophys. Acta *1851*, 1450–1464.

Xu, N., Zhang, S.O., Cole, R.A., McKinney, S.A., Guo, F., Haas, J.T., Bobba, S., Farese, R.V., Jr., and Mak, H.Y. (2012). The FATP1-DGAT2 complex facilitates lipid droplet expansion at the ER-lipid droplet interface. J. Cell Biol. *198*, 895–911.

Xu, D., Li, Y., Wu, L., Li, Y., Zhao, D., Yu, J., Huang, T., Ferguson, C., Parton, R.G., Yang, H., and Li, P. (2018). Rab18 promotes lipid droplet (LD) growth by tethering the ER to LDs through SNARE and NRZ interactions. J. Cell Biol. *217*, 975–995.

Yang, H., Galea, A., Sytnyk, V., and Crossley, M. (2012). Controlling the size of lipid droplets: lipid and protein factors. Curr. Opin. Cell Biol. *24*, 509–516.

Zhao, Y.G., and Zhang, H. (2018). Formation and maturation of autophagosomes in higher eukaryotes: a social network. Curr. Opin. Cell Biol. *53*, 29–36.

Zhao, Y.G., Chen, Y., Miao, G., Zhao, H., Qu, W., Li, D., Wang, Z., Liu, N., Li, L., Chen, S., et al. (2017). The ER-Localized Transmembrane Protein EPG-3/VMP1 Regulates SERCA Activity to Control ER-Isolation Membrane Contacts for Autophagosome Formation. Mol. Cell *67*, 974–989.e6.

STAR★METHODS

KEY RESOURCES TABLE

REAGENT or RESOURCE	SOURCE	IDENTIFIER
Antibodies		
Mouse monoclonal anti-Flag (clone M2)	Sigma-Aldrich	Cat#F1804; RRID: AB_262044
Mouse monoclonal anti-Myc (clone 9E10)	Sigma-Aldrich	Cat#M5546; RRID: AB_260581
Mouse monoclonal anti-His	Sigma-Aldrich	Cat#H1029; RRID:AB_260015
Rabbit polyclonal anti-GFP	Abcam	Cat#ab290; RRID: AB_303395
Mouse monoclonal anti-GFP (clone 7.1 and 13.1)	Roche	Cat#11814460001; RRID: AB_390913
Rabbit polyclonal anti-Sec61β	Abcam	Cat#ab78276; RRID: AB_1566713
Mouse monoclonal anti-Actin (clone 7D2C10)	Proteintech	Cat#60008-1-Ig; RRID: AB_2289225
Rabbit polyclonal anti-DFCP1	ABclonal	Cat#A7527; RRID:AB_2768054
Rabbit polyclonal anti-GPAT4	ABclonal	Cat#A7538; RRID:AB_2769655
Rabbit polyclonal anti-ATG14	Cell Signaling Technology	Cat#5504; RRID: AB_10695397
Rabbit polyclonal anti-ADRP	Proteintech	Cat#15294-1-AP
Mouse polyclonal anti-BSCL2	Abnova Corporation	Cat#H00026580-A02; RRID:AB_627320
Rabbit polyclonal anti-Rab18	Sigma-Aldrich	Cat#SAB4200173; RRID:AB_10638775
Rabbit polyclonal anti-ZW10	Proteintech	Cat#24561–1-AP
Rabbit monoclonal anti-VMP1 (clone D1Y3E)	Cell Signaling Technology	Cat#12929
12 nm colloidal gold AffiniPure goat polyclonal anti-rabbit antibody	Jackson ImmunoResearch Laboratories	Cat#111-205-144; RRID: AB_2338016
Chemicals, Peptides, and Recombinant Proteins		
Wortmannin	Life Technologies	Cat#PHZ1301
Oleic Acid	Sigma-Aldrich	Cat#O7501
DGAT1 inhibitor D1i	TOCRIS	Cat#A922500
Critical Commercial Assays		
RevertAid First Strand cDNA Synthesis Kit	Thermo Fisher Scientific	Cat#K1621
Deposited Data		
Original Data	This paper	N/A
Experimental Models: Cell Lines		
COS7 cells	ATCC	CRL-1651
HeLa cells	ATCC	CCL-2
3T3-L1 preadipocyte cells	ATCC	CL-173
Oligonucleotides		
siRNA NC negative control: 5′-UUCUCCGAACGUGUCACGUTT-3′	This paper	N/A
siRNA Monkey *DFCP1*: 5′-GCGGGACUGAUGAAGCUAUTT-3′	This paper	N/A
siRNA Human *DFCP1*: 5′-GAUCGAAUGUCCUAACUGUTT −3′	This paper	N/A
siRNA Mouse *DFCP1*: 5′-GCCUGGAACUGAUGCAUUUTT-3′	This paper	N/A
siRNA Monkey *BSCL2*: 5′-GGUGUCUGUCUUCCUCUAUTT-3′	This paper	N/A
siRNA Human *BSCL2*: 5′-GGCUCCUUCUACUAUUCCUTT −3′	This paper	N/A
siRNA Monkey *Rab18*: 5′-CCCUGAAGAUCCUCAUCAUTT-3′	This paper	N/A
siRNA Mouse *Rab18*: 5′-GGAGCUUGUUGAGAAGAUCTT-3′	This paper	N/A
siRNA Monkey *FIT2*: 5′-UCAUUGCCCUCACCAACUATT-3′	This paper	N/A
Recombinant DNA		
GFP-DFCP1	This paper	N/A
Flag-DFCP1	This paper	N/A
mCherry-DFCP1	This paper	N/A
DFCP1-RFP	This paper	N/A

(*Continued on next page*)

Continued

REAGENT or RESOURCE	SOURCE	IDENTIFIER
ΔER+FYVE(DFCP1)-GFP (aa 1-415)	This paper	N/A
ER(DFCP1)-GFP (aa 416-543)	This paper	N/A
FYVE(DFCP1)-GFP(aa 585-777)	This paper	N/A
ER+FYVE(DFCP1)-GFP (aa 416-777)	This paper	N/A
GFP-DFCP1(W543A)	This paper	N/A
GFP-DFCP1(C650S, C770S)	This paper	N/A
GFP-Rab18	This paper	N/A
GFP-Rab18(Q67L)	This paper	N/A
GFP-Rab18(S22N)	This paper	N/A
3xMyc-ZW10	This paper	N/A
BSCL2-GFP	This paper	N/A
BSCL2-3xMyc	This paper	N/A
mCherry-HPos	This paper	N/A
ER(DFCP1)+FYVE(FENS)-GFP	This paper	N/A
FYVE(FENS)-TM(CYTOB5)-GFP	Axe et al., 2008	N/A
GFP-LiveDrop	Gift from Junjie Hu	N/A
RFP-Sec61β	Gift from Junjie Hu	N/A
GFP-Sec61β	Gift from Junjie Hu	N/A
ACSL3-GFP	This paper	N/A
GPAT4-GFP	This paper	N/A
DsRed-KDEL	Gift from Junjie Hu	N/A
DGAT2-GFP	Gift from Pingsheng Liu	N/A
3xFlag-FATP1	Gift from Pingsheng Liu	N/A
pEGFP-C1	Clontech	Cat#6084-1
GST-DFCP1	This paper	N/A
GST-Rab18	This paper	N/A
GST-Rab18(Q67L)	This paper	N/A
GST-Rab18(S22N)	This paper	N/A
GST-DFCP1(aa 1-412)	This paper	N/A
GST-DFCP1(aa 412-544)	This paper	N/A
GST-DFCP1(aa 544-777)	This paper	N/A
His-Rab18	This paper	N/A
His-DFCP1	This paper	N/A
Software and Algorithms		
Volocity software	PerkinElmer	N/A
ImageJ	NIH	https://imagej.en.softonic.com/
GraphPad Prism	GraphPad Software	https://www.graphpad.com/

CONTACT FOR REAGENT AND RESOURCE SHARING

Further information and requests for resources and reagents should be directed to and will be fulfilled by the Lead Contact, Hong Zhang (hongzhang@ibp.ac.cn).

EXPERIMENTAL MODEL AND SUBJECT DETAILS

Cell culture

HeLa, COS7 and 3T3-L1 preadipocyte (from ATCC) cells were cultured in medium containing DMEM (SH30022.01B, Hyclone) and 10% FBS (SH30084.03, Hyclone) with penicillin-streptomycin at 37°C and 5% CO_2. None of these cell lines listed above as misidentified or cross-contaminated in the International Cell Line Authentication Committee (ICLAC) database, and all were free of mycoplasma contamination.

Cells were treated with 5 μM wortmannin (PHZ1301, Life Technologies) for 4 hr to inhibit PI(3)P kinase. Cells were incubated with 0.2 mM OA (oleic acid, O7501, Sigma) for the indicated time to induce LD formation. Cells were incubated with 5 μM DGAT1 inhibitor D1i (A922500, TOCRIS) for 6 hr in the presence of OA to inhibit TG synthesis.

METHOD DETAILS

Plasmids

Human DFCP1 cDNA was cloned into pFlag-CMV4 vector, pEGFP-C3 vector, pmCherry-C1 and pTagRFP-N1 vector. ΔER+FYVE(DFCP1)-GFP, ER(DFCP1)-GFP, FYVE(DFCP1)-GFP and ER+FYVE(DFCP1)-GFP were generated by cloning DFCP1 (aa 1-415), DFCP1 (aa 416-543), DFCP1 (aa 585-777), and DFCP1 (aa 416-777) into pEGFP-N1 vector, respectively. GFP-DFCP1(W543A) and GFP-DFCP1(C650S, C770S) were generated by PCR-based mutagenesis from GFP-DFCP1. Human Rab18 was cloned into pEGFP-C1 vector. GFP-Rab18(Q67L) and GFP-Rab18(S22N) were generated by PCR-based mutagenesis from GFP-Rab18. Human cDNA encoding BSCL2 was inserted into pEGFP-N1 vector. BSCL2-3xMyc was generated by adding 3xMyc to the C terminus of BSCL2. mCherry-HPos was constructed by cloning HPos into pmCherry-C1 vector. ER(DFCP1)+FYVE(FENS)-GFP was generated by inserting human FENS (aa 276-358) into ER(DFCP1)-GFP. GFP-HPos was kindly provided by Dr. Albert Pol (Institut d'Investigacions Biomèdiques August Pi i Sunyer). FYVE(FENS)-TM(CYTOB5)-GFP was kindly provided by Dr. Nicholas T. Ktistakis (Babraham Institute). GFP-LiveDrop, GFP-Sec61β and RFP-Sec61β were kindly provided by Dr. Junjie Hu (Institute of Biophysics, Chinese Academy of Sciences).

Transfection and RNA interference

Transfection of plasmids was carried out with Lipofectamine 2000 (12566014, Life Technologies). Cells were transfected with NC or siRNA oligos, which were purchased from GenePharma using Lipofectamine RNAiMAX (13778150, Life Technologies), and cultured for 72 hr before analysis. RNAi sequences were listed in KEY RESOURCES TABLE.

Lipid droplet staining assay

Cells were washed with PBS three times and fixed with 4% PFA for 20 min. After washing with PBS, LDs were stained with LipidTOX (1:1000, H34476, Life Technologies) for 15 min at room temperature. Coverslips were mounted with DAPI in 50% glycerol and examined under a confocal microscope (LSM 880 Meta plus Zeiss Axiovert zoom, Zeiss) with a 63 × oil-immersion objective lens (Plan-Apochromatlan, Zeiss) and a camera (Axiocam HRm, Zeiss).

Membrane fractions

After washing with PBS 3 times, cells were scraped into 1 mL ice cold buffer E (20 mM HEPES, pH 7.4, 250 mM sucrose, 1 mM EDTA and protease inhibitor cocktail), 1 mL pH 11.5 buffer (100 mM sodium carbonate, pH 11.5) or 1 mL high salt buffer (10 mM Tris-HCl, pH 8.0/ 0.5 M NaCl). Cells were then homogenized with 100 strokes in a Dounce homogenizer (K885300-0002, Thermo Fisher). After being centrifuged at 20,000 g, the homogenates (total sample) were incubated for 30 min at 4°C and then ultracentrifuged at 200,000 g for 1 hr at 4°C. The supernatants were transferred to a new tube and the pellet was resuspended in the same volume of the original buffer. Total sample, supernatant and pellet fractions were resuspended in SDS-sample buffer and analyzed by immunoblotting.

LD mobility

Cells were seeded into glass-bottom dishes (801001, NEST) and transfected with NC or siRNA oligos for 48 hr and the indicated plasmids for the last 24 hr. After LipidTOX staining (1:1000, H34475, Life Technologies) for 15 min, cells were imaged at 37°C and 5% CO_2 using a 100 × objective (CFI Plan Apochromat Lambda, NA 1.45, Nikon) with immersion oil on an inverted fluorescence microscope (Eclipse Ti-E, Nikon) with a spinning-disk confocal scanner unit (UltraView, PerkinElmer). Image sequences were captured every 1 s for ~200 s. The images were cropped to find discrete items and track objects, and the mean velocity of objects of interest was analyzed with Velocity software (PerkinElmer).

LD purification

Cells were washed with ice-cold PBS, and then harvested by centrifugation at 3,000 g for 10 min (Sigma 12150-H). Cells were then washed twice with 30 mL buffer A (25 mM tricine, 250 mM sucrose, pH 7.8), and resuspended in 30 mL buffer A. Cells were homogenized by passing through a French pressure cell at 100 MPa, 4°C. The sample was centrifuged at 3,000 g for 10 min. The supernatant fraction was transferred to a SW40 tube. 2 mL buffer B (20 mM HEPES, 100 mM KCl, 2 mM $MgCl_2$, pH 7.4) was added on top of the supernatant and then centrifuged at 182,000 g for 1 h at 4°C (Beckman SW40). The LD fraction was transferred to a 1.5 mL Eppendorf tube, washed with buffer B three times and then dissolved with chloroform-acetone (1:1) to precipitate proteins. After centrifugation at 20,000 g for 10 min, the pellet was dissolved with 2 × SDS sample buffer and denatured at 95°C for 5 min for further analysis.

Co-immunoprecipitation assays

After transfection with the indicated plasmids for 24 hr, COS7 cells were washed 3 times and dispersed in lysis buffer (50 mM HEPES, pH 7.4, 150 mM NaCl, 1 mM EDTA, 1% Triton X-100 and protease inhibitor cocktail) for 30 min. After the lysates were centrifuged at 20,000 g for 10 min at 4°C, the supernatants were transferred to a new tube. 50 μl of each supernatant were saved as input. For GFP-Trap assays, the rest of the supernatant was immunoprecipitated by GFP-Trap agarose beads (gta-20, ChromoTek) for 1.5 hr at 4°C. After washing, the samples were resuspended in SDS-sample buffer and analyzed by immunoblotting. For IP of endogenous protein, antibody was premixed with the rest of the supernatant for 2 hr at 4°C, and then incubated with protein G beads (Roche) for 1 hr at 4°C. After washing, the samples were resuspended in SDS-sample buffer and analyzed by immunoblotting.

Protein expression and purification

GST-Rab18 and GST-DFCP1 were generated by inserting PCR-amplified human genes into pGEX-6P-1 vector to produce GST-tag proteins. GST-Rab18(Q67L) and GST-Rab18(S22N) were generated by PCR-based mutagenesis from GST-Rab18. GST-DFCP1(aa 1-412), GST-DFCP1(aa 412-544) and GST-DFCP1(aa 544-777) were generated by truncating GST-DFCP1. A modified version of pET-32a (Novagen) with Trx-His_6-tag at the N terminus was used to generate His-Rab18. Human DFCP1 was cloned into pET-28a to generate His-DFCP1. Recombinant proteins were expressed in *Escherichia coli* BL21-CodenPlus (DE3) and purified using Sepharose 4B beads (GST-tagged protein, GE Healthcare). After loading onto desalting columns (GE Healthcare), proteins were finally eluted with 1 × PBS buffer. GST-Rab18(Q67L) and GST-Rab18(S22N) used buffer containing 50 mM Tris-HCl (pH 8.0), 500 mM NaCl and 2 mM DTT.

In vitro pulldown assays

GST or GST-tagged protein (20 μg) and His-tagged protein (50 μg) were incubated with 20 μL GST beads in 500 μL pulldown buffer (1 × PBS, 0.1% Triton X-100) for 1 hr at 4°C. After washing 3-5 times with pulldown buffer, proteins were resuspended in 5 × SDS-sample buffer and visualized by immunoblotting. GST-DFCP1 protein was incubated with protease inhibitor cocktail (Roche, B14003) for 1 hr at 4°C. For GST-tagged mutants of Rab18, the pulldown buffer (20 mM HEPES (pH 7.4), 200 mM NaCl, 0.1% Triton X-100) was supplemented with 5 mM GTP for GST-Rab18(Q67L) or 5 mM GDP for GST-Rab18(S22N) and 5 mM Mg^{2+}. To examine the interaction between His-Rab18 and GST-tagged DFCP1 fragments, 5 mM GTP and 5 mM Mg^{2+} were included in the pulldown buffer.

Electron microscopy

Cells ($1x10^6$) were transfected with NC and/or indicated siRNA oligos for 72 hr. For cells transfected with plasmids expressing GFP-tagged proteins, GFP-positive cells were sorted by flow cytometry (BD FACSAria IIIu). Collected cells were fixed with 2.5% glutaraldehyde in PBS overnight at 4°C. After 3 washes in the same buffer, cells were post-fixed in 1% OsO_4 and 0.05% potassium ferrocyanide for 45 min. Cells were then washed with water and dispersed in thiocarbohydrazide (TCH) solution for 30 min at room temperature. Then cells were washed again and incubated with 1% OsO_4 for 45 min at room temperature. After washing, cells were further dehydrated by a graded series of ethanol solutions and embedded in epoxy resin.

For OTO (ferrocyanide reduced osmium tetroxide post-fixation, thiocarbohydrazide-osmium liganding) staining, samples were subjected to graded dehydration and embedding, then ultrathin sections were stained with uranyl acetate and lead citrate.

For DAB staining, cells were transfected with a construct expressing an APEX2 fusion protein. Cells were sorted by flow cytometry and then fixed with 2.5% glutaraldehyde in PBS overnight at 4°C and rinsed 3 × 10 min in PBS. Cells were treated with a freshly diluted solution of 0.5 mg/ml (1.4 mM) DAB tetrahydrochloride for 12 min, then rinsed 3 × 10 min with chilled buffer. Cells were post-fixed in 1% OsO_4 for 90 min at room temperature. Cells were rinsed 3 × 10 min in chilled distilled water, and then placed in chilled 2% aqueous uranyl acetate (Electron Microscopy Sciences) for 1 hour. A 120 kV electron microscope (H-7650B, Hitachi) was used at 80 kV. Images were captured with an AMT CCD camera (XR-41) using Digital Micrograph software at room temperature.

3D-structured illumination microscopy

3D-structured illumination microscopy (3D-SIM) images of COS7 cells were acquired on a DeltaVision OMX V3 imaging system (GE Healthcare) with a × 100/1.40 NA oil objective (Olympus UPlanSApo), solid-state multimode lasers (488, 405 nm, 561nm) and electron-multiplying CCD (charge-coupled device) cameras (Evolve 512 × 512, Photometrics). Serial Z stack sectioning was done at 125 nm intervals for SIM mode. To obtain optimal images, immersion oils with refractive indices of 1.512 were used for COS7 cells on glass coverslips. The microscope was routinely calibrated with 100 nm fluorescent spheres to calculate both the lateral and axial limits of image resolution. SIM image stacks were reconstructed using softWoRx 6.1.1 (GE Healthcare) with the following settings: pixel size 39.5 nm; channel-specific optical transfer functions; wiener filter constant 0.0010; discard negative intensities background; drift correction with respect to first angle; custom K0 guess angles for camera positions. The 3D reconstruction of the GFP-DFCP1- and LipidTOX-stained LD surface was processed using Imaris x64 8.1.4 software.

Immunoelectron microscopy

Cells were fixed in buffer containing 2% paraformaldehyde, 0.2% glutaraldehyde and Na cacodylate (pH 7.4) for 2 hr at 37°C. After dehydration and embedding in acrylic resin (LR White), 70 nm ultrathin sections were mounted on nickel grids, and then the nickel grids were incubated in 1% BSA diluted with PBS containing the indicated antibodies at 4°C overnight. After washing with 0.2% BSA

diluted with PBS, the nickel grids were probed with gold-conjugated particles in 1% BSA diluted with PBS for 2 hr at room temperature. The ultrathin sections were then stained and examined. Images were captured by a Gatan-832 digital camera on a 120 kV Jeol electron microscope (JEM-1400) at 80 kV.

FRAP experiment

LDs were stained with LipidTOX for 15 min and then fluorescence recovery after photobleaching (FRAP) experiments were performed on a confocal microscope (LSM 880 Meta plus Zeiss Axiovert zoom, Zeiss) using a 63 × oil immersion objective lens (Plan-Apochromatlan, Zeiss) and a camera (Axiocam HRm, Zeiss) at room temperature. A defined region of interest was photobleached at full laser power at 488 nm (100% power, 20 iterations). Fluorescence intensity was normalized to the pre-bleach intensity. Image intensity was measured by Mean ROI on a confocal microscope (LSM 880 Meta plus Zeiss Axiovert zoom, Zeiss) and further analyzed by Prism (GraphPad).

Grazing incidence SIM

After seeding on 25-mm coverslips, COS7 cells were transfected with NC or siRNA oligos for 48 hr, and transfected with the indicated plasmids for the last 24 hr. Before imaging, COS7 cells were stained with LipidTOX for 15 min.

The grazing incidence structured illumination microscopy (GI-SIM) apparatus was built based on an inverted fluorescence microscope (IX83, Olympus, Japan). In this system, the light beams from a laser combiner equipped with 488 nm (500 mW, Coherent, Genesis Max 488-500 STM), and 560 nm (1W, MPB Communications, VFL-P-500-560) lasers are passed through an acousto-optic tunable filter (AOTF; AA Quanta Tech, AOTFnc-400.650-CPch-TN), which is used to dynamically select the excitation laser and control its power inputting into the backward light path. The output beam from the AOTF is then expanded to a 1/e diameter of 12 mm and sent to a phase-only modulator consisting of a polarizing beam splitter, an achromatic half-wave plate (HWP; Bolder Vision Optik, BVO AHWP3), and a ferroelectric spatial light modulator (SLM; Forth Dimension Displays, SXGA-3DM). The light diffracted by the grating pattern displayed on the SLM passes through a polarization rotator consisting of a liquid crystal cell (LC; Meadowlark, SWIFT) and an achromatic quarter wave plate (QWP; Bolder Vision Optik, BVOAQWP3), which rotates the linear polarization of the diffracted light so as to maintain the *S*-polarization necessary to maximize the pattern contrast for all pattern orientations.

Images were captured with an Olympus 1.7-NA objective under the physiological conditions of 37°C and 5% CO_2. Three raw images were acquired at successive phase steps of 0, 1/3, and 2/3 for each illumination time-point. This process was repeated with the standing wave excitation pattern rotated ± 120° with respect to the first orientation, for a total of nine raw images. In this work, we used an imaging speed of 1 frame per 4, 5 or 10 s at 50 W/cm^2 excitation intensity, and continuously imaged ~200 time-points.

QUANTIFICATION AND STATISTICAL ANALYSIS

Immunoblotting, in-vitro pulldown and Co-IP results are representative of three independent experiments. Dead/unhealthy cells were excluded from analysis. The cells or images for analysis were randomly chosen. No specific randomization method was applied. The statistical parameters, including n, SEM and SD, are reported in the Figures and corresponding Figure Legends. Statistical analysis was performed in Microsoft Excel, Prism (GraphPad) and ImageJ. Statistical significance was calculated by one-way ANOVA analysis. A *P value* < 0.05 was considered significant. For comparison of the percentage of LDs in contact with the ER, the Chi-square test was used to test significance. No statistical methods were used to predetermine the sample size, or to determine whether the data met the assumptions of the statistical approaches used.